University of Reading

# *Ultra-slow self-similar coarsening of physical fibrillar gels formed by semiflexible polymers*

Article

Published Version

Creative Commons: Attribution-Noncommercial 3.0

Open Access

Kröger, M., Luap, C. and Ilg, P. ORCID: https://orcid.org/0000-0002-7518-5543 (2025) Ultra-slow self-similar coarsening of physical fibrillar gels formed by semiflexible polymers. Soft Matter, 21 (15). pp. 2803-2825. ISSN 1744-683X doi: 10.1039/D4SM01479K Available at https://centaur.reading.ac.uk/120537/

It is advisable to refer to the publisher's version if you intend to cite from the work. See Guidance on citing.

To link to this article DOI: http://dx.doi.org/10.1039/D4SM01479K

Publisher: Royal Society of Chemistry

All outputs in CentAUR are protected by Intellectual Property Rights law, including copyright law. Copyright and IPR is retained by the creators or other copyright holders. Terms and conditions for use of this material are defined in the End User Agreement.

www.reading.ac.uk/centaur

University of Reading

**CentAUR**

Central Archive at the University of Reading

Reading's research outputs online

Volume 21
Number 15
21 April 2025
Pages 2751–2968

# Soft Matter

rsc.li/soft-matter-journal

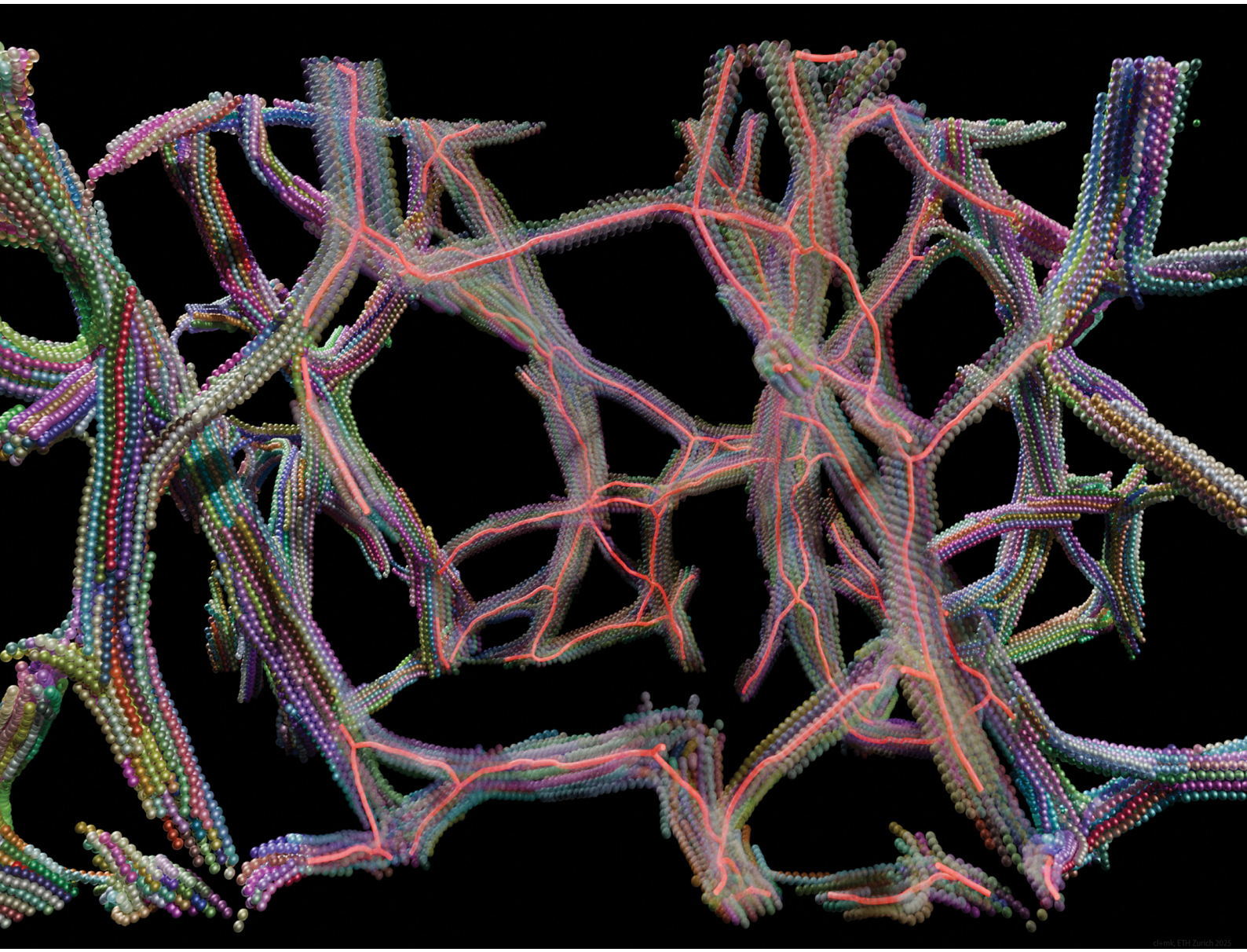

ISSN 1744-6848

ROYAL SOCIETY OF CHEMISTRY

**PAPER**
Martin Kröger, Clarisse Luap and Patrick Ilg
Ultra-slow self-similar coarsening of physical fibrillar gels formed by semiflexible polymers

20 YEARS ANNIVERSARY

Soft Matter

PAPER

View Article Online
View Journal | View Issue

Check for updates

Cite this: *Soft Matter*, 2025, **21**, 2803

# Ultra-slow self-similar coarsening of physical fibrillar gels formed by semiflexible polymers†

Martin Kröger, *[ab] Clarisse Luap*[c] and Patrick Ilg *[d]

Biopolymers tend to form fibrils that self-assemble into open network structures. While permanently crosslinked flexible polymers are relatively well understood, structure–property relationships of open networks and pseudo-gels formed by bundles of biopolymers are still controversial. Here we employ a generic coarse-grained bead-spring chain model incorporating semiflexibility and cohesive nonbonded interactions, that forms physical instead of chemical crosslinks. For flexible chains, the cohesive forces lead to the formation of a droplet phase while, at the same concentration, stiffer chains form bundles that self-assemble into percolated networks. From comprehensive molecular dynamics simulations we find that the reversible crosslinks allow for permanent relaxation processes. However, the associated reorganization of the filamentous network is severely hindered, leading to aging of its topology. Based on morphometric analyses, the ultra-slow coarsening in these systems is proven to be self-similar, which implies a number of scaling relations between structural quantities as the networks age. The percolated structures are characterized by different dynamic regimes of slow, anomalous diffusion with highly non-Gaussian displacements. Relaxation dynamics is found to become extremely slow already on moderate length scales and further slowing down as coarsening proceeds. Using a minimal model supported by observations on filament rupture and rearrangement, our study helps to shed light on various interrelated structural and dynamical aspects of coarsening nonergodic systems relevant for fibrous networks, pseudo-gels, and physical fibrillar gels.

Received 13th December 2024,
Accepted 30th January 2025

DOI: 10.1039/d4sm01479k

rsc.li/soft-matter-journal

Open Access Article. Published on 26 February 2025. Downloaded on 6/10/2025 3:11:34 PM.
This article is licensed under a Creative Commons Attribution-NonCommercial 3.0 Unported Licence.

## 1 Introduction

Semiflexible macromolecules are ubiquitous in nature.[1] A prominent example is cellulose, a semiflexible glucose polymer. As the main constituent of plant fiber, it is the most abundant organic compound on earth. DNA and proteins are other examples of important semiflexible biopolymers. Under typical conditions, many of these monofilaments form bundles[2] or fibrillar structures that assemble into transient networks with physical, *i.e.* reversible crosslinks.[3–5] These networks show remarkable properties such as strain stiffening and negative normal stresses,[6] which are rather different from networks of permanently crosslinked flexible chains that have been intensively studied using traditional network theories and simulation. For example, structure–property relationships were investigated for cellulose hydrogels, with mechanical properties found to depend on fibril length instead of concentration as expected from traditional network theories.[7] The network structure formed by physically crosslinked semiflexible polymers has an important influence on their mechanical properties.[8–10]

For a better understanding of these structures, it is helpful to note that they are prepared experimentally *e.g.* using a change of temperature, ionic strength, or pH.[1,11] Theoretically, the resulting gelation *via* bundling and network formation from suspensions of semiflexible polymers is interpreted as emerging from spinodal decomposition and kinetic arrest.[3,12–15] The associated reorganizations of the network can be extremely slow, in some cases exceeding several days.[16] The corresponding phenomena of slow coarsening dynamics with very long correlation lengths are known as "anomalous aging" since the time evolution and relaxation dynamics differs markedly from the more intensively studied glassy systems.[17] Nonergodicity and anomalous aging has been observed in a broad range of different systems such as amyloid fibrils,[1,18] methylcellulose,[16] alginate gels[19] and colloidal gels.[17] Considerable work is ongoing to extend traditional theoretical approaches to capture such biological soft matter systems.[9,20]

[a] *Computational Polymer Physics, Department of Materials, ETH Zurich, 8093 Zurich, Switzerland. E-mail: mk@mat.ethz.ch*
[b] *Magnetism and Interface Physics, Department of Materials, ETH Zurich, 8093 Zurich, Switzerland*
[c] *Independent researcher, 8049 Zurich, Switzerland. E-mail: clarisse.luap@alumni.ethz.ch*
[d] *School of Mathematical, Physical, and Computational Sciences, University of Reading, Reading, RG6 6AX, UK. E-mail: p.ilg@reading.ac.uk*

† Electronic supplementary information (ESI) available: Displacements, aging and ultra-slow coarsening, end-to-end vector correlation, Torquato's pore size distribution, intermediate scattering function, additional snapshots, movies, Github repository. See DOI: https://doi.org/10.1039/d4sm01479k

Open Access Article. Published on 26 February 2025. Downloaded on 6/10/2025 3:11:34 PM.
This article is licensed under a Creative Commons Attribution-NonCommercial 3.0 Unported Licence.

Here, we focus on reversible networks of semiflexible chains without permanent crosslinks for which classical theories can not readily be applied.[5] Although such transient structures are theoretically fascinating and highly relevant *e.g.* for food systems or protein-based filaments, they remain underexplored.[9] Several fundamental questions on the structure and dynamics of these networks stay unclear.[8] For cellulose derivatives often used in food systems, for example, fibrillar structures with a characteristic mean diameter of about 5 to 30 nm are observed experimentally.[11,21,22] From cryo-TEM imaging and small-angle neutron scattering (SANS), the fibril mean diameter was found to be rather independent of molecular weight, temperature and concentration, but increasing with increasing bending stiffness.[11,21] From detailed molecular simulation, these fibrils were either explained as stacked ring structures[23] or lengthwise aggregation of chain molecules.[24] Different X-ray scattering experiments and cryo-TEM images seem to be more consistent with the latter scenario, suggesting axially oriented semi-crystalline chains forming the core of the fibril, interspersed with less dense regions.[25,26] Small angle X-ray scattering experiments (SAXS) experiments were used to study fibrils formed from short peptides. The change in the characteristic slope in the scattering functions was consistent with a model of thick cylinders.[27] While scattering experiments on dilute solutions of semiflexible chains are well understood,[28,29] corresponding results for networks of semiflexible chains provide valuable structural information that, however, is sometimes difficult to interpret. One difficulty is that experimentally prepared networks are often found to be spatially inhomogeneous. Mesh sizes estimated from permanent networks of rodlike particles give the right order of magnitude measured for the more compact regions, whereas much larger values are found for the more open regions.[30]

Networks of semiflexible chains show intriguing dynamics that is challenging to study not least because of their non-ergodic nature.[1,9] For example, non-diffusive compressed exponential relaxation was observed in amyloid fibrils from dynamic light scattering experiments.[31] These findings hint at structural heterogeneities of the network, but the origin of the relaxation remains unclear. Additionally, uncertainties persist regarding the different dynamic regimes and anomalous diffusion in transient networks of semiflexible chains,[32] their underlying microscopic origins, and their connection to resulting mechanical properties.[9]

In general, computer simulations can help to address these questions as they offer detailed insight into structural as well as dynamical properties. They allow to detect microscopic mechanisms accompanying the coarsening process. The majority of simulations in this field seem to employ detailed atomistic or moderately coarse-grained models to investigate specific systems.[23,24,27,33,34] Because of the computational complexity of these systems only few computational studies appeared to date on the self-assembly process of semiflexible filaments and the dynamics of their networks.[34] To overcome these limitations, several coarse-grained models have been proposed that differ considerably in the level of detail retained.[33] Recently, promising multi-scale simulations have appeared that address the mechanisms of self-assembly in methylcellulose.[24] Rather than targeting such a specific chemistry, we aim at exploring universal properties of transient networks of semiflexible chains. As has been noted,[5,15] (i) the bundling of semiflexible chains into fibrils, (ii) the characteristic and rather uniform fibril diameters, and (iii) network topologies appear to be rather similar for different types of polymers. Effective attractions arise in many biopolymeric systems as a result of depletion forces.

With this in mind, we here employ a generic model of semiflexible polymers in terms of multibead-spring chains with bending stiffness and short-range attraction, building on the so-called Kremer–Grest[35] and FENE-CB[36–38] models. Models with qualitative similarities have been used in the past to study microphase separation in fibrillar gels,[39] the phase behavior of semiflexible attractive chains, showing a liquid–vapor coexistence region for low enough temperatures or strong enough cohesive energies,[40] and the formation of fibrous bundles,[41,42] which then assemble to form a temporary network.[15] For a two-dimensional version of the model, network structures were investigated in detail, distinguishing percolated from disintegrated networks.[43] Other recent studies used a similar model to investigate the network structure and their tensile properties, finding that high strength networks have high densities and that the cohesive energy is the most important parameter for their mechanical response.[44,45] While bead-spring models are an extremely versatile model for various polymeric systems,[46] we note in passing that other coarse-grained models have sporadically been used to study aspects of semiflexible polymer networks, such as an extended fluid particle model for the evolution and stability of networks,[47] and a discrete element method for the study of gelation, bundles, and pore size distributions.[48]

Studying the aging model system requires special care not only due to the loss of ergodicity[1] which introduces a dependence on the preparation conditions, but also due to the additional effect of the waiting time since system preparation.[49] Several simulation studies on semiflexible polymer networks artificially arrested aging by introducing sticky beads or permanent crosslinks or quenching the temperature to zero.[44,45,48] Here, we avoid such drastic interventions and study the structure, dynamics, and aging of a self-assembling, physically crosslinked semiflexible polymer system. We pay special attention to carefully prepare the systems to follow the aging process as far as possible.[12,50] To address the lack of ergodicity, we typically investigate 10 statistically independent samples, and we investigate the influence of waiting time ($t_w$) and bending stiffness ($\kappa$) on static and dynamic properties.

## 2 Model system

The model studied here is a semiflexible, anharmonic multibead-spring model that differs from the celebrated KG model[35] for linear polymer chains in melts only with respect to bending energy and interaction cutoff, and is conveniently implemented using LAMMPS[51] (LAMMPS script available in Section S8, ESI†).

 This journal is © The Royal Society of Chemistry 2025

Open Access Article. Published on 26 February 2025. Downloaded on 6/10/2025 3:11:34 PM.
This article is licensed under a Creative Commons Attribution-NonCommercial 3.0 Unported Licence.

### 2.1 Model equations and parameters

The usually $N_c = 1000$ linear, monodisperse bead-spring chains, each consisting of $N = 30$ identical beads, $N_b = N_c N$ beads in total, are contained in a periodic simulation box with volume $V$, at bead number density $\rho = N_b/V$ and temperature $T$. All permanently bonded beads along the linear chains interact *via* the radially symmetric finitely extendable nonlinear elastic (FENE) potential,[52]

$$U_{\mathrm{FENE}}(b) = -\frac{k}{2}R_0^2 \ln\left[1 - (b/R_0)^2\right], \qquad (1)$$

with spring coefficient $k = 30$ and maximum extension $R_0 = 1.5$, where $b$ denotes a bond length. This potential serves as a rather poor approximation to the inverse Langevin function at large extensions,[53] but is typically employed. All pairs of beads interact *via* a truncated, radially symmetric Lennard-Jones (LJ) potential,

$$U_{\mathrm{LJ}}(r) = 4\varepsilon_b(r^{-12} - r^{-6} - r_c^{-12} + r_c^{-6}), \quad r \le r_c, \qquad (2)$$

and $U_{\mathrm{LJ}}(r) = 0$ for $r > r_c$, where $\varepsilon_b = 1$ and $r_c = r_{\min} = 2^{1/6}$ for all permanently bonded beads, $\varepsilon_b = 3$ for all nonbonded beads, while $r_c$ for all nonbonded beads remains a model parameter. In eqn (2), $r = |\mathbf{r}_i - \mathbf{r}_j|$ denotes a spatial distance between a pair of beads $i$ and $j$. A pair of nonbonded beads can be regarded as having formed a temporary (reversible) bond as long as the distance between the two beads is below $r_c$. The energy penalty to break such a temporary bond defines a cohesion energy

$$E_{\mathrm{coh}} = -U_{\mathrm{LJ}}(r_{\min}) = \frac{\left(2 - r_c^6\right)^2 \varepsilon_b}{r_c^{12}} \qquad (3)$$

that ranges between zero and $\varepsilon_b = 3$, depending on the choice of $r_c$. Eqn (3), employing $\varepsilon_b = 3$, can also be inverted as $r_c = \left[6/\left(3 - \sqrt{3E_{\mathrm{coh}}}\right)\right]^{1/6}$.

Finally, each triplet of adjacent permanently bonded beads interacts *via* the cosine bending potential[36–38]

$$U_{\mathrm{bend}} = \kappa(1 - \mathbf{u}_i \cdot \mathbf{u}_{i+1}) \qquad (4)$$

where the bending stiffness $\kappa$ is a key model parameter, and $\mathbf{u}_i = \mathbf{b}_i/b_i$ (with $\mathbf{b}_i = \mathbf{r}_{i+1} - \mathbf{r}_i$) is a unit bond vector, if beads $i$ and $i + 1$ are permanently bonded to each other. The model of interacting semiflexible bead-spring chains is shown schematically in Fig. 1(a), together with the interaction potentials (1) and (2) and the cohesive energy (3). The sketch also indicates permanent (FENE) bonds between neighboring monomers as well as temporary bonds due to LJ interactions between beads that are currently within a cut-off radius $r_c$.

Polymer chains are assumed to be embedded in a solvent which is modeled implicitly. The quality of the solvent is related to the cohesive energy $E_{\mathrm{coh}}$, while dynamic effects are captured in the free-draining approximation by friction forces acting on all beads. To this end, a Langevin thermostat is applied to ensure a constant temperature $T$. We choose $T = 1$ and set $k_B = 1$, so that $\kappa/k_BT = \kappa$ in our case, and we write $\kappa/k_BT$ only if it serves to highlight a dependency on temperature. Otherwise, LJ units are used throughout.

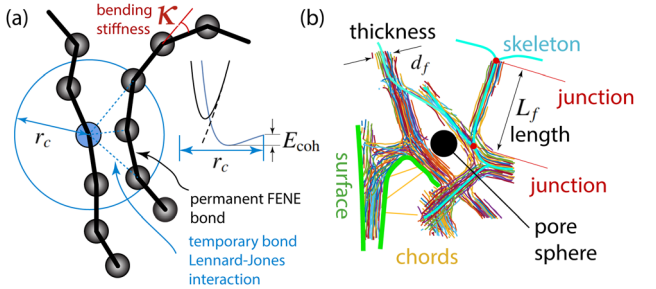


Fig. 1 (a) Sketch of the interaction potentials at work. The $E_{\mathrm{coh}}$ is directly related to a cutoff distance $r_c$, defining temporary, reversible bonds, that are used – together with the permanent FENE bonds – to define a cluster. The inset shows the LJ (blue) and FENE (dashed black) potentials, as well as the sum of FENE and LJ potentials (black). (b) Geometrical quantities characterizing the network composed of semiflexible chains: the skeleton (obtained by a thinning algorithm), which we use to extract junctions, the length and thickness of filamentous strands (edges), the surface required to define chord lengths and pore radii.

### 2.2 Preparation of model systems

Systems are generated by placing $N_c$ semiflexible chains with initial bond length $b_{\mathrm{init}} = 1$ and with persistence length $L_p = -b_{\mathrm{init}}/\ln[\mathscr{L}(\kappa/k_BT)]$, involving the Langevin function $\mathscr{L}(x) = \coth(x) - x^{-1}$, but without overlap (minimum bead–bead distance 0.85)[54] into a periodic simulation box whose volume is determined by either (i) an initial bead number density $\rho_{\mathrm{init}} = 0.02$ for the NPT ensemble, or (ii) $\rho_{\mathrm{init}} = 0.05$ for the NVT ensemble simulations. The equations of motion resulting from the mentioned potentials are then integrated using classical thermo- and barostats (NPT only) using an integration time step $\Delta t = 0.005$. For case (i) the system is equilibrated within the NPT ensemble until its pressure is fluctuating about zero; at this time the system has reached a number density $\rho$ that may largely deviate from $\rho_{\mathrm{init}}$, and is moreover insensitive to $\rho_{\mathrm{init}}$ due to the relatively low $\varepsilon_b = 3$ that we have chosen. The simulations within the NPT ensemble suggest to use $\rho = 0.05$ for the NVT ensemble simulation. Here, for case (ii), the short relaxation stage (duration $10^3$) is followed by a measurement stage of duration $10^5$. Long runs up to $t_w = 2.1 \times 10^6$ were performed for $\kappa \in \{10, 50, 75\}$. The begin of the measurement stage defines waiting time $t_w = 0$. During these stages, we keep $\rho$ fixed and integrate the equations of motion using a Langevin thermostat with friction coefficient $\zeta = 0.5$, following previous works.[35,55] Movies E to G and E+ to G+ (ESI†) show show selected systems during the short relaxation and early measurement stage, and during the coarsening stage, respectively.

## 3 Results and discussion

We study in detail structural characteristics as well as dynamic properties of cohesive semiflexible polymers using the model described in Section 2. Fig. 2 serves to demonstrate the richness of structures that our simple model is able to capture at a single temperature, using chains of identical length. It shows projections of snapshots of various systems at a bead number density

Open Access Article. Published on 26 February 2025. Downloaded on 6/10/2025 3:11:34 PM.
This article is licensed under a Creative Commons Attribution-NonCommercial 3.0 Unported Licence.

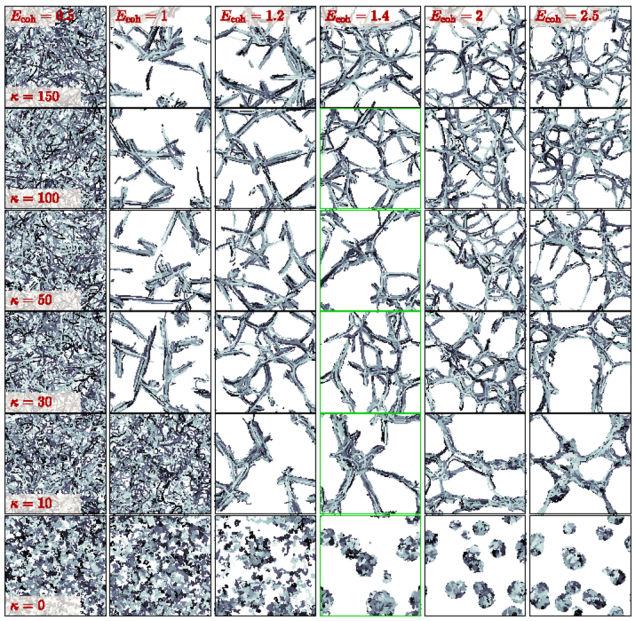


Fig. 2 Projected snapshots at waiting time $t_w = 10^4$ *versus* bending stiffness $\kappa$ (vertical) and cohesive energy $E_{coh}$ (horizontal) for configurations with $N_c = 1000$ chains, $N = 30$ beads per chain, bead number density $\rho = 0.05$, temperature $T = 1$, subjected to periodic boundary conditions. Shown are projected slices, 50% of the whole system. Each chain has its own gray scale value. This work focuses on the green framed parameter region with $E_{coh} = 1.4$ and $\kappa \leq 100$.

of $\rho = 0.05$. This density we determined from a series of NPT simulations for pressure $P = 0$ for intermediate values of bending stiffness $\kappa$. For better comparison we then fixed $\rho = 0.05$ in NVT simulations for all systems and $\kappa$ values investigated. The systems shown in Fig. 2 were simulated for a relatively short time, up to time $t_w = 10^4$ since system preparation. Varying the cohesive energy $E_{coh}$ (horizontally) and bending stiffness $\kappa$ (vertically) is found to lead to different structures. For small $E_{coh} \lesssim T$, isolated chains are found that become more straight with increasing bending stiffness. Increasing $E_{coh}$ leads to cluster and structure formation. For low $\kappa$, these clusters tend to be more compact, while larger $\kappa$ together with cohesive attractions leads to open, network-like structures.

To carefully study these structures and resulting properties, from now on we fix a representative value of the cohesive energy ($E_{coh} = 1.4$) and focus on the influence of the bending stiffness $\kappa$ on static and dynamic properties. With the chosen value of $E_{coh}$, we make sure to include compact as well as open structures in our study (green framed regime in Fig. 2).

### 3.1 Initial observations

Snapshots of representative system configurations with $N_c = 1000$ chains, polymerization degree $N = 30$, thus $N_b = N_c N = 30\,000$ beads in total are shown at a late stage of a typical run in Fig. 3. Different panels in the figure correspond to different values of bending stiffness $\kappa$. These figures are thus not only close-up three-dimensional versions of the corresponding panels of Fig. 2, but show those systems after considerable longer times $t_w$. For rather flexible chains, $\kappa \lesssim 5$, droplets are formed by several coiled chains. For more rigid chains, $\kappa \gtrsim 5$, strongly bent configurations are energetically too unfavorable: droplets mixed with short, near-cylindrical bundles ($\kappa = 5$) as well as system-spanning networks of long, fibrillar bundles ($\kappa \gtrsim 10$) are formed. Thus, the snapshots suggest both an ordering and a percolation transition as the bending stiffness increases. These observations are in agreement with Monte–Carlo simulation of very small systems that found a transition from amorphous aggregates to polymer bundles at $\kappa \approx 6$.[41] For

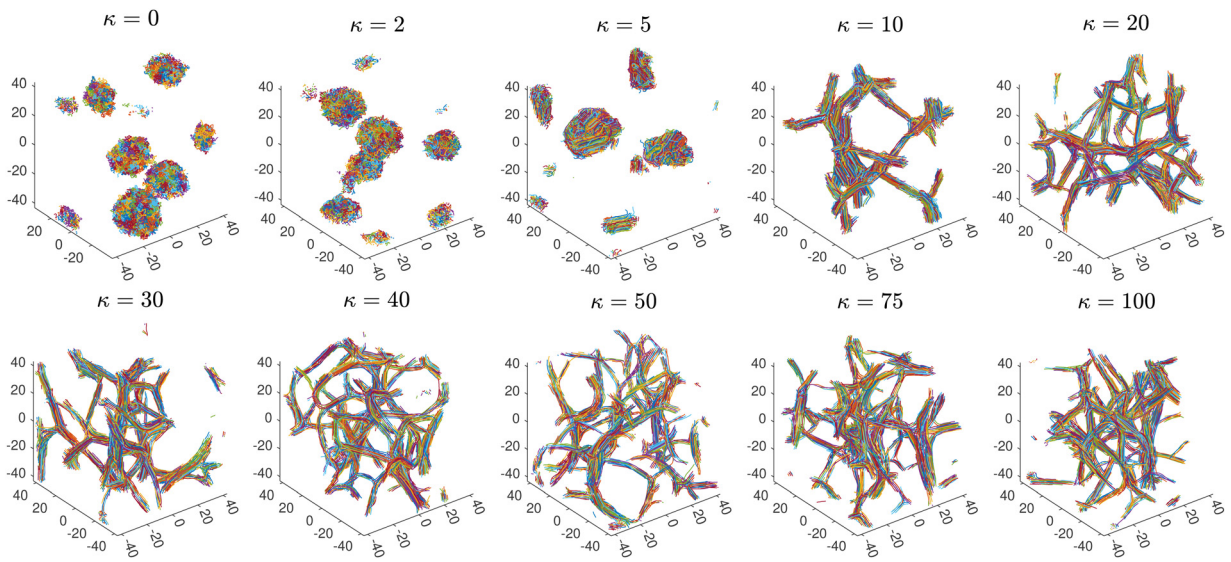


Fig. 3 Snapshots for a homologous series of systems with different bending stiffness $\kappa$ mentioned in the panels ($N_c = 1000$ chains, polymerization degree $N = 30$, bead number density $\rho = 0.05$, temperature $T = 1$, cohesive energy $E_{coh} = 1.4$) at waiting time $t_w = 10^5$ since system preparation. Each chain has its own color. Larger systems ($N_c = 50\,000$) have been studied as well, most time-dependent quantities are reliably obtained from the small systems already.

 This journal is © The Royal Society of Chemistry 2025

Open Access Article. Published on 26 February 2025. Downloaded on 6/10/2025 3:11:34 PM.
This article is licensed under a Creative Commons Attribution-NonCommercial 3.0 Unported Licence.

a few (2 out of 10 in each case) samples within the transition regime we also observed thick filaments percolated in one dimension for $\kappa = 5$, and networks for $\kappa = 10$ percolated in two dimensions (Fig. S14, ESI†). We will come back to these points later.

As a first proxy for structure evolution, we monitor the mean pair energy ($e_{pair}$) and mean bending energy per particle ($e_a$) as a function of $t_w$. The pair energy $e_{pair}$ is defined as the mean LJ energy (2) per bead. As can be seen from Fig. 4, $e_{pair}$ and $e_a$ both decrease with time as expected for equilibration. As a decreasing $e_a$ reflects local bending stiffening, chains tend to straighten out in the course of $t_w$. The decrease of $e_{pair}$ suggests an increase in local ordering and decrease in surface area. When plotting these two quantities on a linear time scale, Fig. 4(a) and (b), one might be inclined to conclude that equilibration is mainly achieved. However, closer inspection and using a logarithmic time scale (Fig. 4(c) and Fig. S7, ESI†) reveals a very slow ongoing relaxation with a relaxation time that increases significantly with system age.

Recall that aging and ultra-slow coarsening have been observed in several network-forming soft matter systems.[12–14,16–19,47,49,50,56,57] The essential absence of complete relaxation in these systems has been attributed to phase separation and quasi-arrested spinodal decomposition, explaining the similar phenomenology observed in rather different systems.[12,57,58] In particular, spinodal decomposition has been identified as the driving force for bundling and network formation in polymeric systems similar to the one studied here.[3,14,15] In the following, we study and discuss the aging and coarsening behavior. As an interesting first observation, Fig. 4(d) shows a linear relation between the pair and bending energy during relaxation, indicating that coarsening proceeds along certain rules.

### 3.2 Structure analysis and static properties

We begin by analyzing the structures that are formed for different values of $\kappa$ and the corresponding static properties. In view of the ultra-slow ongoing relaxation, we perform all structural analysis at different $t_w$.

**3.2.1 Single chain structure factors and persistence lengths.** The static structure factor is a fundamental quantity routinely determined in both scattering experiments and simulations, as it encapsulates key structural information. Experimentally, it offers a unique method for probing features across different length scales, particularly in systems that are too small to be studied directly through microscopy techniques.

We first present results for the isotropic single-chain structure factor, $S_{sc}(q)$, as function of wave number $q$. Experimentally, $S_{sc}$ can be measured through small-angle neutron scattering (SANS) on samples where a small fraction of polymer chains have been selectively labeled. In simulations, the static structure factor can conveniently be extracted from bead positions. See Section 5.1 for details and in particular eqn (8) for a definition of $S_{sc}(q)$. Fig. 3(a) shows $S_{sc}$ obtained for various values of the bending stiffness $\kappa$. Data averaged over two different ranges of waiting times $t_w$ are quasi indistinguishable. As $\kappa$ increases we see a transition from a near-random walk behavior ($S_{sc} \sim q^{-2}$) to an extended range of $q$ values where $S_{sc} \sim q^{-1}$ shows the typical scaling of rod-like objects. It is remarkable that despite chain–chain interactions, $S_{sc}$ can still be described very well by the scattering function of the discrete wormlike chain (WLC) model (for details see Section 5.1). However, the required values of persistence lengths differ from the local persistence lengths $\ell_p$ that are inferred from the bending energy $e_a$ (Section 5.2).

To confirm this observation, we analysed directly two single-chain properties: the mean-square end-to-end distance $\langle R^2 \rangle$ and the gyration radius $R_g$. For the WLC model, these quantities are given in terms of the number of beads per chain $N$ and the global persistence length $L_p$ (see Section 5.2 and Fig. S10, ESI†). Values for $L_p$ extracted from the ratio $\langle R^2 \rangle / R_g^2$ are shown in Fig. 6 (time series in Fig. S7, ESI†) together with those extracted from the fits of the single chain structure factor. The latter are systematically smaller but follow the same trend: the effective global persistence length initially increases approximately linearly with $\kappa$, before crossing over to a much slower increase for $\kappa \gtrsim 20$. The local effective persistence length $\ell_p$ evaluated from the bending energy agree with those from $R_g$ for $\kappa \gtrsim 2$, but clear differences are seen for stiffer chains where bending energies imply larger values of $\ell_p$ compared to $L_p$'s from the gyration radius. For our systems, we suspect that the scale-dependency of the persistence length of chains within the fibrous networks may be caused by the formation of junctions connected by strands whose lengths do not exceed $L_p$ by far.

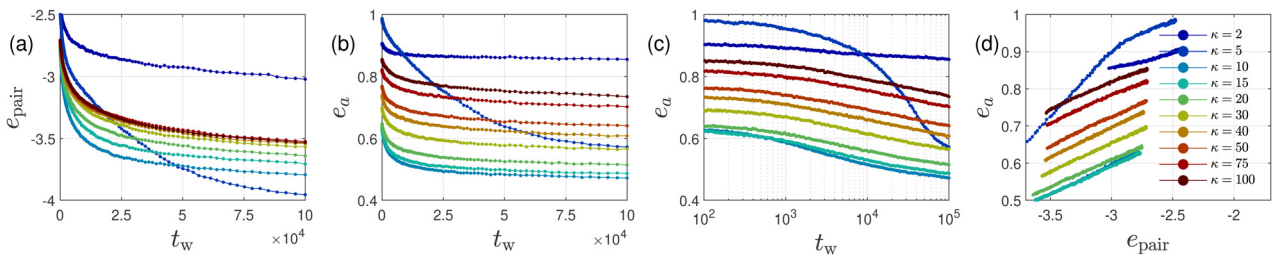


Fig. 4 Energies during aging. Panel (a) shows the pair energy per bead, $e_{pair}$, as a function of waiting time $t_w$ since system preparation for various values of the bending stiffness $\kappa > 0$ shown in the legend of panel (d). Panel (b) shows the bending energy per bead, $e_a$, *versus* $t_w$, while panel (c) shows the same data on a semilogarithmic scale. Panel (d) shows a parametric plot of $e_a(t)$ *versus* $e_{pair}(t)$. Time thus increases from right to left in (d). From $e_a$ we extract a local persistence length $\ell_p$, shown in Fig. 6. While all percolated networks ($\kappa \geq 10$) follow a similar trend, the energetics of the unordered spherical ($\kappa \leq 2$) and little cylindrical bundles ($\kappa = 5$, Movie H, ESI†) phases is markedly different. Plots extending to later times $t_w = 2.1 \times 10^6$ are available in Fig. S7 (ESI†).

Open Access Article. Published on 26 February 2025. Downloaded on 6/10/2025 3:11:34 PM.
This article is licensed under a Creative Commons Attribution-NonCommercial 3.0 Unported Licence.

**3.2.2 Structure factor.** The full static structure factor $S(q) = N_b^{-1} \sum_{i,j=1}^{N_b} \langle e^{i\mathbf{q}\cdot\mathbf{r}_{ij}} \rangle$ as defined in eqn (7) accounts for all beads in the system, regardless of bond topology. Fig. 5(b) presents $S(q)$ for the same range of bending stiffness $\kappa$ as in Fig. 5(a). At first glance, two different families of curves can be distinguished in Fig. 5(b): (i) the one for rather flexible chains ($\kappa \leq 5$) forming droplet phases and (ii) the one for stiffer chains $\kappa \geq 10$ forming percolated fibrous networks. These findings corroborate earlier observations from the snapshots in Fig. 3 which indicate a transition from a droplet- to a network-forming phase as $\kappa$ increases from $\kappa = 5$ to $\kappa = 10$.

At large scattering vectors ($q \geq 7$), both systems exhibit the usual diffuse scattering peaks reminiscent of the bead-bead intra and inter-chain correlations.

For droplet systems, the $S(q)$ curves show no distinct peaks or fringes, indicating that the dense globular droplets are quite irregular in shape and/or polydisperse. However, fringes of small amplitudes are detectable in individual samples if averaged over the last 100 time units only (data not shown). Due to the limited size of our systems, the Guinier regime ($qR_g < 1$) is not reached and no correlation peaks corresponding to a characteristic droplet–droplet distance are observed. In the probed (intermediate) $q$ range, the scattering curves follow a Porod-like behavior $S(q) = K_p/q^4$, and are therefore dominated by the scattering arising from the sharp density change at the droplet interfaces. For spherical droplets of radius $R$, this regime appears for $q > q_c$ where $q_c \propto 1/R$. The proportionality

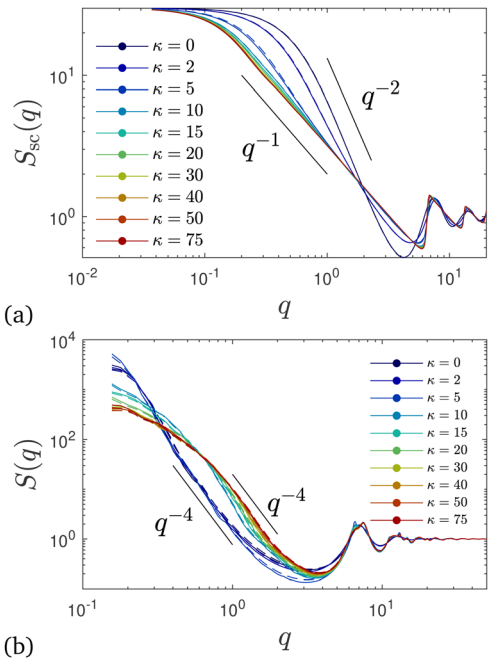


Fig. 5 Structure factors. (a) $S_{sc}(q)$ and (b) $S(q)$ averaged over $t_w \in [0,10^5]$ (dashed) and $t_w \in [5 \times 10^4, 10^5]$ (solid). In panel (a) power laws $q^{-1}$ (rod-like) and $q^{-2}$ (Gaussian) have been added to guide the eye. (b) The Porod $q^{-4}$-regimes, signaling well defined interfaces in both the unpercolated ($\kappa < 10$, spherical and cylindrical clusters) and percolated regimes ($\kappa \geq 10$, filamentous networks) are highlighted.

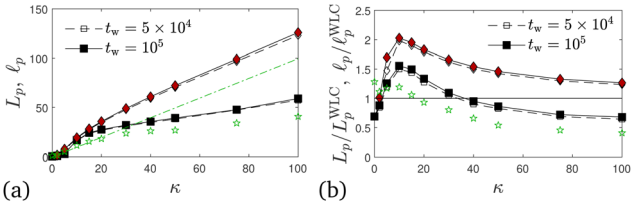


Fig. 6 Persistence lengths *versus* $\kappa$ at two different waiting times $t_w$. (a) Global $L_p$ extracted from the ratio $\langle R^2 \rangle / R_g^2$ (black squares), using the discrete WLC expression (10), local $\ell_p$ obtained from the specific bending energy $e_a$ (red diamonds), and $L_p$ estimated upon fitting the $S_{sc}$ by the WLC model (green pentagons). Dot-dashed green line $L_p^{WLC} = \ell_p^{WLC} = -b/\ln[\mathscr{L}(\kappa/k_BT)]$ for the ideal WLC has been added to guide the eye. (b) Same data as shown in (a), here relative to the the ideal WLC. Global $L_p$'s obtained using the bond length $b$ and $R_g^2$, or alternatively $\langle R^2 \rangle$ alone are basically identical to those obtained from the ratio. The single chain structure factor $S_{sc}(q)$ (Fig. 5) is very well approximated by the WLC structure factor, using $L_p$ values that are slightly below the ones obtained from the ratio.

constant $K_p$, setting the level of $S(q)$ in the Porod regime, is given in our case by $K_p = 2\pi\rho_f^2 A_f/N_b$, where $\rho_f$ is the bead number density in the dense polymer phase and $A_f$ its total surface area.[59]

For the percolated network structures, the shape of scattering curves is consistent with that expected for polydisperse cylindrical objects. A narrower Porod regime is observed ($q_c \propto 1/d$ with $d$ denoting a cylinder diameter) whose onset slightly shifts to higher $q$ with increasing stiffness, indicating a slight decrease in fiber diameters which saturates at large $\kappa$. The levels of $S(q)$ in the Porod regime are significantly higher than those for the droplet systems, in agreement with the higher interfacial area of the fibrous network structures. In Fig. 5, the structure factors averaged over two different ranges of waiting times $t_w$ since system preparation are nearly undistinguishable. Yet a slight increase in the Porod constant over time is hinted. Overall, the structure factors data allow to clearly classify our systems into two types of structures: globular and cylindrical. However, the limited low-$q$ range and the absence of prominent features in the curves make it challenging to extract precise quantitative structural information.

**3.2.3 Real space structural analysis.** While the time-averaged structure factors capture essential, experimentally accessible parameters such as $R_g$, $L_p$, $\rho_f$, $A_f$ in reciprocal space, our simulation provides access to the full temporal evolution of not only these, but of additional structural quantities directly in real space. A qualitative picture readily emerges based on animated sequences of the chain trajectories (see Section S7, Movies A–J, ESI†). They provide a visual impression about the self-assembly of chains into bundles and the formation and evolution of the network or droplet structures. To quantitatively capture key aspects of these observations for further analysis, we extract the number of clusters, strands, junctions and loops, critical bonds, the mean strand length and bundle thickness, chord length and pore size distributions, using methods such as a skeleton-algorithm (a thinning algorithm, the skeleton follows the centerline of the filaments), Voronoi decomposition, Euler's topological identities and the Cauchy–Crofton formula. Fig. 1(b)


This journal is © The Royal Society of Chemistry 2025

Open Access Article. Published on 26 February 2025. Downloaded on 6/10/2025 3:11:34 PM.
This article is licensed under a Creative Commons Attribution-NonCommercial 3.0 Unported Licence.

schematically shows the skeleton as well as these other characteristic elements of the networks. For better readability, we here focus on the results obtained and only sketch the methods employed. Full details of all methods used here are given in Section 5.

First, our cluster analysis (Section 5.4.1) confirms a percolation transition where a single, system-spanning infinite cluster ($C = 1$) is formed for semiflexible chains with $\kappa \geq 10$ (Fig. 22). For more flexible chains with $\kappa \leq 5$, several droplets of isolated smaller clusters of coiled chains are seen. Those clusters tend to coagulate with time for $\kappa \leq 2$, while short bundles of aligned chains tend to be more stable for $\kappa = 5$. Note that the precise location of the percolation transition also depends on the value of the cohesive energy $E_{\mathrm{coh}}$ and moves to larger $\kappa$ as $E_{\mathrm{coh}}$ decreases. While there are no critical (load-bearing) bonds[60] (Section 5.4.1) for the droplet systems, the number of critical bonds in the percolated networks ($\kappa \geq 10$) is quite insensitive to $\kappa$. The system at $\kappa = 30$ attains the largest number (roughly 600) of critical bonds and may thus be envisioned as the most mechanically stable system under study (this prediction could be scrutinized *e.g.* by mechanical tests).

Fig. 7(a)–(f) show the ensemble-averaged strand length $L_f$ and thickness $d_f$ (Section 5.4.4), number of edges $E$, junctions $J$, and loops $L_\circ$ (Section 5.4.3), and the mean pore size $r_{\mathrm{pore}}$ introduced by Gelb and Gubbins[61] (Section 5.4.5), respectively, as a function of the bending stiffness $\kappa \geq 10$ for percolated systems at two selected values of the waiting time, $t_{\mathrm{w}} = 5 \times 10^4$ and $t_{\mathrm{w}} = 10^5$. All but the pore size have been obtained with the help of skeletons (Section 5.4.2, Fig. S3, ESI†), whose flexible multibead strands (of mean contour length $L_f$) follow the centerlines of the filamentous bundles, until they terminate at one- (dangling ends) or higher-functional junctions (see Fig. 1(b) for a sketch). Each skeleton bead is easily characterized by its functionality, and from the knowledge of the number $n_f$ of skeleton beads with given functionality $f$, and the number $C$ of clusters, one has direct access to the number of edges, junctions, vertices, and loops without inspecting the network further. We observe that $L_f$, strand diameter $d_f$ ($\simeq$mean thickness of the polymeric strands centered at the skeleton) and pore radius $r_{\mathrm{pore}}$ decrease monotonically with increasing bending stiffness (at given $t_{\mathrm{w}}$) until reaching a plateau for large $\kappa$. The number of edges, junctions, and loops exhibit the opposite trend. The stiff systems therefore exhibit more junctions, thinner filaments, and a smaller pore radius compared with the flexible systems at comparable age, but upon aging the stiffer systems much further, their topological characteristics tend to become similar to those of the more flexible, younger systems.

For an ideal network free of dangling ends and solely composed of three-functional junctions the number of junctions equals the number of vertices, the number of edges is 3/2 times the number of junctions, $E/J = 3/2$, and the number of loops is $L_\circ = C + E/3$. As mentioned, our coarsed percolated networks all exhibit a single infinite cluster, $C = 1$. From the quantities displayed in Fig. 7(c), (d) and (f) one can infer the number of dangling ends, $n_1 = C + E - J - L_\circ$, which is relatively small, and a mean functionality of junctions, $\bar{f}_J = (2E - n_1)/J$,

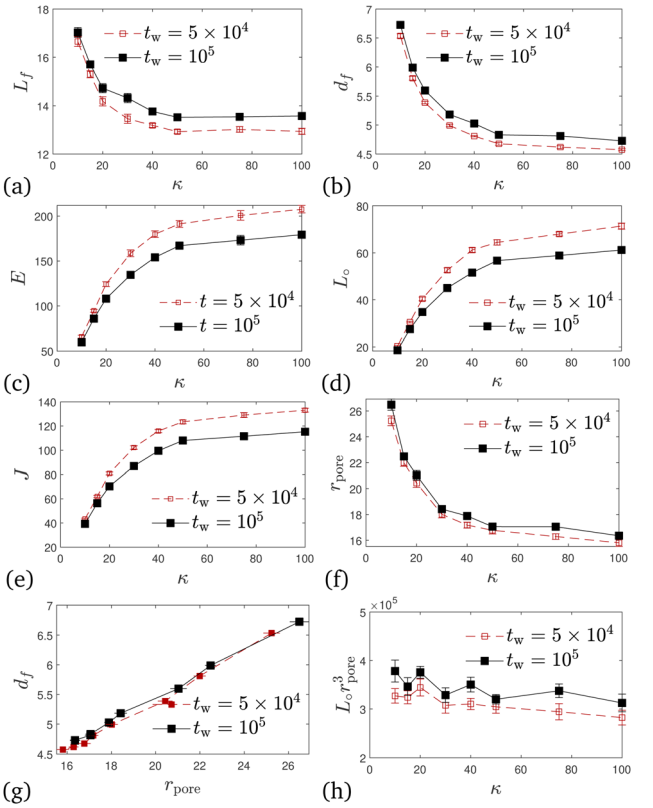


Fig. 7 Effect of stiffness on network topology and mean pore radius. Various quantities characterizing network structures are shown for percolated systems with $\kappa \geq 10$. Panels (a)–(f) show the mean filament length $L_f$ and diameter $d_f$, the number of edges $E$, loops $L_\circ$, junctions $J$, and the mean pore radius $r_{\mathrm{pore}}$, respectively, as a function of bending stiffness $\kappa$. In panel (g), we plot the mean filament diameter for different $\kappa$ parametrically *versus* the mean pore radius. Panel (h) shows the combination $L_\circ r_{\mathrm{pore}}^3$ as a function of $\kappa$. Full black squares correspond to waiting times of $t_{\mathrm{w}} = 10^5$, open red squares to $t_{\mathrm{w}} = 5 \times 10^4$.

close to three. To be specific, we find at $t_{\mathrm{w}} = 10^5$ that the ratio of dangling ends to three-fold junctions, $n_1/n_3$, monotonically decreases from about 0.07 at $\kappa = 10$ to 0.04 at $\kappa = 100$, while the ratio of four-fold to three-fold junctions, $n_4/n_3$, monotonically and weakly increases with $\kappa$ from about 0.01 to 0.03 over the same $\kappa$ range and there is a negligible amount of higher-functional junctions. In more quantitative terms, for the ratio $E/J$ we obtain a nearly constant value of $\approx 1.535$ over the whole range of $\kappa$ values, while $L_\circ/(1 + E/3)$ moderately increases from 0.93 to 0.97 between $\kappa = 10$ and $\kappa = 100$. For this reason, our networks are near-ideal three-functional at $t_{\mathrm{w}} = 10^5$, and they approach this stage in a manner that is captured by the time series of functionalities (Fig. S4, ESI†). Even though systems with different $\kappa$ age at different rates, the mentioned trends are unaffected by the choice of $t_{\mathrm{w}}$.

Our results concerning $d_f$ are in qualitative agreement with earlier simulations of a similar model system.[45] In comparison to the static structure factor shown in Fig. 5, the quantities $L_f$, $d_f$, $L_\circ$ and also $r_{\mathrm{pore}}$ show more clear differences for the two values of $t_{\mathrm{w}}$. Mass conservation arguments can be used, as shown in Section 5.5.4, to heuristically derive a scaling

Open Access Article. Published on 26 February 2025. Downloaded on 6/10/2025 3:11:34 PM.
This article is licensed under a Creative Commons Attribution-NonCommercial 3.0 Unported Licence.

relation between the mean filament diameter $d_f$ and the mean pore size,

$$d_f \sim r_{\mathrm{pore}}. \tag{5}$$

Fig. 7(g) shows a parametric plot of the mean filament diameter $d_f$ *versus* the mean pore radius $r_{\mathrm{pore}}$. For all values $\kappa \geq 10$ and different waiting times, we find that our data follow the scaling relation (5) reasonably well. We note that a corresponding relation for a two-dimensional transient network of semiflexible chains was also found to hold rather well.[43] In addition, we observe from Fig. 7(h) that the product of the number of loops and the pore volume, $L_c r_{\mathrm{pore}}^3$, is approximately constant. Since $L_c/J$ reflects the total amount of loops per branch point including primary and higher-order loops, its value does help to judge about the modulus or fracture energies, which are presumably better captured by the cycle rank,[62] or the above-mentioned amount of critical bonds.

The values shown in Fig. 7 provide descriptions of the network structure in terms of mean quantities, and thus do not allow us to draw conclusions about possible heterogeneities. Therefore, we show in Fig. 8(a) and (b) the weighted distribution of filament lengths $L_f$ and diameters $d_f$, respectively, for selected values of the bending stiffness $\kappa$. We find that not only the mean value of $L_f$ remains approximately constant for $\kappa \gtrsim 40$ (see Fig. 8(a)), but the whole distribution, positively skewed, hardly changes in this regime as $\kappa$ increases. For the filament diameter $d_f$ on the other hand, the probability distribution is more Gaussian and moves to lower values as $\kappa$ increases, approaching a limiting distribution only at higher values. Both distributions are relatively broad.

Within the same spirit, in Fig. 9, we show the pore size distribution G-$P_{\mathrm{pore}}^{\mathrm{cum}}(r)$, *i.e.* the cumulative probability that the largest sphere, containing a randomly chosen point within the void space, and not overlapping with any of the beads, has a radius smaller or equal than $r$. For more information on this quantity see Section 5.4.5. For small values of $\kappa$, the system is unpercolated and the distributions have to be interpreted with care. For larger $\kappa$, the vast majority of pores have a radius between around 10 and 20. Together with the smooth increase of G-$P_{\mathrm{pore}}^{\mathrm{cum}}(r)$ we conclude that the networks formed do not show pronounced heterogeneities. We also observe that the mean pore radii $r_{\mathrm{pore}}$ very slightly get larger with increasing waiting time (Fig. S7, ESI†), in agreement with Fig. 7(f). For comparison, Torquato's[63] cumulative T-$P_{\mathrm{pore}}^{\mathrm{cum}}(r)$, defined in Section S4 (ESI†), is shown in Fig. S9 (ESI†). The T-$P_{\mathrm{pore}}^{\mathrm{cum}}(r)$ is known to underestimate the pore radius,[64] but is much less time-consuming to extract with high accuracy. While the pore size distributions do not reveal any qualitative peculiarities, they will help us to demonstrate self-similarity during ultra-slow coarsening.

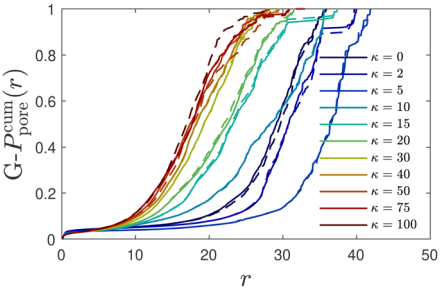


Fig. 9 Pore radii. Cumulative pore size distribution G-$P_{\mathrm{pore}}^{\mathrm{cum}}(r)$ defined in Section 5.4.5 is shown for different values of $\kappa$ as indicated in the legend. Dashed and solid lines correspond to averages over $t_w \in [0,10^5]$ and $t_w \in [5 \times 10^4, 10^5]$, respectively.

Another important, convenient measure of the characteristic length scales of a network is given by the so-called chord length distribution (Section 5.4.6).[65] Roughly speaking, the chord length $s$ is the distance between two consecutive network-pore interfaces along a virtual line through the system.[50,57,66] Fig. 10(a) shows the weighted chord length distribution $\mathscr{C}_1(s)$ of the dense polymeric phase for several values of the bending stiffness $\kappa$. The corresponding weighted chord length distribution of the void space $\mathscr{C}_0(s)$ has been extracted and analyzed as well (Fig. 23). In the droplet phase for $\kappa \leq 5$, $\mathscr{C}_1(s)$ shows a pronounced peak at small $s$ ($s \approx 2$), a weaker and broader peak at larger $s$ ($s \approx 10\ldots20$), followed by a relatively long tail (data not shown). The broad peak can be related to the typical size of droplets (Fig. 3). In the network-forming phase for $\kappa > 10$, the shape of the chord length distribution $\mathscr{C}_1(s)$ changes to a unimodal shape. The location and height of the peak are found to be rather insensitive to the precise value of $\kappa$ in this regime. We note that the most probable chord length decreases weakly with increasing $\kappa$ from about $s \approx 7$ ($\kappa = 10$) to $s \approx 4.5$ ($\kappa = 100$) and is, within numerical uncertainties, identical with the mean filament thickness $d_f$ (Fig. 7b). This finding perfectly supports the conclusion that our percolated systems contain mainly near-cylindrical filaments with $L_f > d_f$.[65] We note that Fig. 10(a) corresponds to a particular time $t_w = 10^5$. The time-dependence and remaining panels of Fig. 10 will be discussed next.

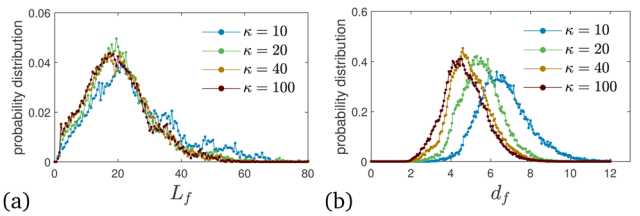


Fig. 8 Polydispersity of filamentous bundles. Probability distribution of filament lengths $L_f$ and diameters $d_f$, for selected $\kappa$, collected within the time frame $t_w \in [5 \times 10^4, 10^5]$.

### 3.3 Ultra-slow coarsening and self-similarity

As we have seen in Section 3.2, various structural quantities show a weak dependence on the waiting time $t_w$ since system preparation and do not seem to have fully reached steady state during the simulation time window. In this section we study this relaxation and the associated aging phenomenon more closely.

Fig. 11 shows a sequence of snapshots for a typical system with $\kappa = 50$ (see Fig. S2 for corresponding snapshots for $\kappa = 10$, ESI†). The snapshots already suggest a coarsening of the

 This journal is © The Royal Society of Chemistry 2025

Open Access Article. Published on 26 February 2025. Downloaded on 6/10/2025 3:11:34 PM.
This article is licensed under a Creative Commons Attribution-NonCommercial 3.0 Unported Licence.

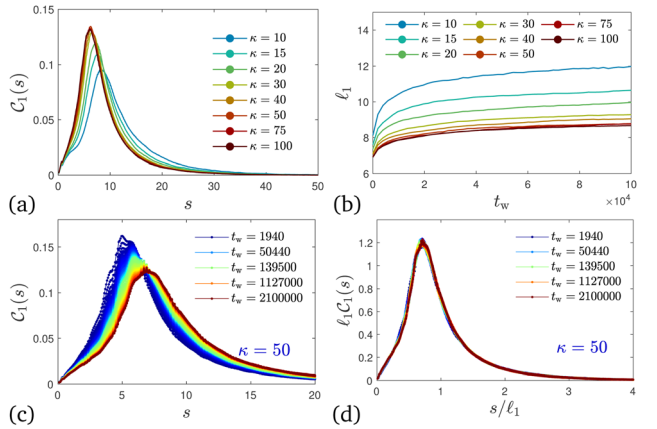


Fig. 10 Chord lengths and self-similarity. (a) Weighted distribution $\mathscr{C}_1(s)$ of chord lengths are shown at $t_w = 10^5$ for various values of bending stiffness $\kappa$ as indicated in the legend. (b) Mean weighted chord length $\ell_1 \equiv \int s\mathscr{C}_1(s)\mathrm{d}s / \int \mathscr{C}_1(s)\mathrm{d}s$ as a function of time $t_w$ since system preparation. Panel (c) shows the weighted chord length distribution $\mathscr{C}_1(s)$ for $\kappa = 50$. Distributions are recorded at various times $t_w$, increasing from blue to red as indicated by selected $t_w$ in the legend. Panel (d) shows the same data as (c) but rescaled as $\ell_1\mathscr{C}_1(s)$ *versus* $s/\ell_1$. The corresponding plots for the distribution $\mathscr{C}_0(s)$ are shown in Fig. S23 (ESI†).

network structure with increasing waiting time $t_w$. To study the ongoing coarsening more quantitatively, we monitor the polymer surfaces and skeletons, as illustrated in Fig. 12. We note that our polymer surfaces look rather similar to SEM or AFM images of biopolymers.[7,31,56,67,68] Fig. 13(a), (b) and 10(b) show the time evolution of the skeleton and surface-based characteristics, including the mean filament length $L_f$ and diameter $d_f$ and mean weighted chord length $\ell_1$ since system preparation, respectively. The very slow relaxation seen in Fig. 4 can thus be attributed to an ultra-slow coarsening process of the network structure, as suggested by Fig. 11 and 12. Indeed, mass conservation arguments detailed in Section 5.5.4 suggest the scaling relation (5) to hold during late stages of coarsening, which we find to be satisfied to a good degree. Therefore, we conclude that coarsening mainly consists of filaments very slowly becoming thicker with pores very slowly getting larger.

We can monitor the ultra-slow coarsening also *via* the weighted chord length distribution of the dense phase, $\mathscr{C}_1$. As seen in Fig. 10(c) and (d), coarsening in the droplet and network-forming phase is associated with a slow shift of $\mathscr{C}_1$ to larger chord lengths, in agreement with the ultra-slow

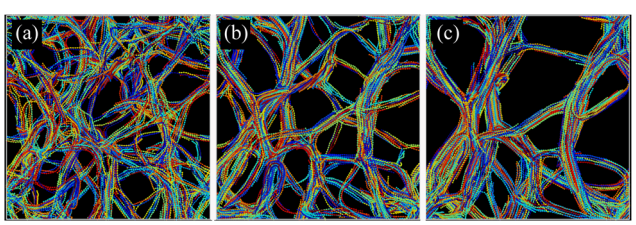


Fig. 11 Network coarsening. Selected snapshots (orthographic projections) with $\kappa = 50$ ($N_c = 1000$ chains) at waiting times (a) $t_w = 1940$, (b) $t_w = 5 \times 10^4$, and (c) $t_w = 10^5$. Each chain has its own color.

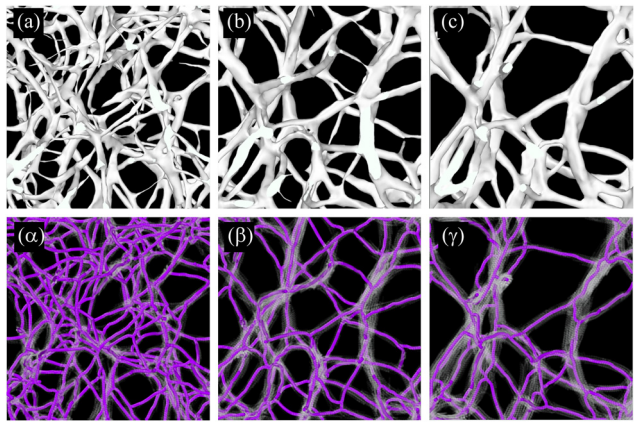


Fig. 12 Accessible polymer surfaces and skeletons, morphometric analysis. Orthographic projections of (a)–(c) polymer surface and corresponding (α-γ) skeletons (purple lines) for the three configurations shown in Fig. 11. In (a)–(c) the polymer surfaces are obtained using Ovito's[69] "construct surface mesh" modifier with probe sphere radius 1.5 and smoothing level 4. In (α-γ) the system beads are rendered as semi-transparent gray spheres.

increase of the mean weighted chord length $\ell_1$ over time seen in Fig. 10(b). The curves for $\kappa > 10$ in Fig. 10(b) are well reproduced (up to within 2%) by a logarithmic growth law (see Section 5.5.2). Extrapolating this law to a hypothetical final state of a single droplet or cylindrical filament would mean that $\ell_1$ keeps rising significantly up to times of the order of $t = 10^{15}$ to $10^{20}$! In other words, the mean $\ell_1$, if averaged over all times up to time $t_{end}$, increases by about 15% if $t_{end}$ is increased by one order of magnitude. Using $\ell_1(t)$ as a time-dependent characteristic length scale of the network, we can rescale $\mathscr{C}_1(s;t)$ at different times $t$ onto a single master curve, $\ell_1(t)\mathscr{C}_1(s;t) = f_1(s/\ell_1(t))$ (for details see Section 5.5.3, ESI†). Fig. 10(d) shows the rescaled curves for different times $t_w$. A very good collapse of all data shown in Fig. 10(c) onto a single master curve $f_1(x)$ is observed. The functional form of the universal master curve $f_1(x)$ for the network-forming phase is well represented by the analytical expression given in eqn (29). Similar observations are made based on the weighted chord length distributions of the void space $\mathscr{C}_0 > 0$ (Fig. 23). When scaled with the corresponding mean chord length of the void space $\ell_0(t)$, its master curve $f_0(x)$ is captured by the analytical expression (27). We can use the functional form of $f_0(x)$ to

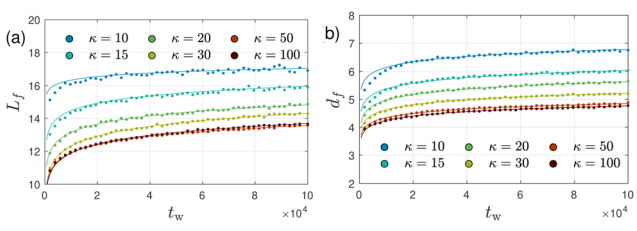


Fig. 13 Aging of filamentous bundles. Waiting time dependence of (a) mean filamentous strand length $L_f$ and (b) diameter $d_f$ for selected values of $\kappa$ as indicated in the legend. Symbols represent simulation results, while solid lines show logarithmic fits.

Open Access Article. Published on 26 February 2025. Downloaded on 6/10/2025 3:11:34 PM.
This article is licensed under a Creative Commons Attribution-NonCommercial 3.0 Unported Licence.

extrapolate $\mathscr{C}_0$ beyond the box size. This procedure allows us to estimate the moments of the distribution including the mean weighted and unweighted chord lengths, $\ell_0$ and $l_0$, free of finite-size effects.

Furthermore, we find that the scaled filament length $L_f/\ell_1$ and thickness $d_f/\ell_1$ as well as the scaled mean pore size $r_{\mathrm{pore}}/\ell_1$ are essentially time-independent when early stages of coarsening are discarded. Therefore, we conclude that the ultra-slow coarsening observed here is self-similar. A corresponding conclusion has recently been reached for a network-forming colloidal suspension based on the weighted chord length distribution $\mathscr{C}_0$ of the void spaces.[12]

### 3.4 Coarsening mechanism

In an effort to better understand the ultra-slow coarsening mechanism, we propose a minimal model of fibril breaking and rearrangement. See Fig. 14 for a sketch. In this model, a representative fibril between two network junctions is modeled as a bundle of parallel chains that can diffuse longitudinally and independently of each other. The number $c$ of chains in the bundle is proportional to the fibril cross section. When all chain ends meet, the bundle breaks into two parts that each join a different fibril, leading to a corresponding increase in fibril cross sections. For fibrils with larger cross sections and correspondingly more chains, the probability that all chain ends meet is reduced and so is bundle breakage, leading to an increase in rupture time $\tau_{\mathrm{rup}} \propto N^{c-1}$. Employing a simple rate equation $\mathrm{d}c/\mathrm{d}t_{\mathrm{w}} \propto c/t_{\mathrm{w}}$, this model predicts $c(t_{\mathrm{w}}) \approx a + b\ln(t_{\mathrm{w}})$, *i.e.* a logarithmic growth for the mean number of chains in the cross-section of a fibril, eqn (20), derived in Section 5.5.1. Therefore, the minimal model motivates the use of logarithmic growth laws to describe our data on coarsening. We find that logarithmic growth laws describe well not only the coarsening of the mean filament length and diameter as shown in Fig. 13, but also other structural quantities such as the mean pore size, chord lengths, as well as pair and bending energies, with relative deviations of only a few percent. Some of these other quantities are shown together with fits to logarithmic growth laws in Fig. S5–S7 (ESI†).

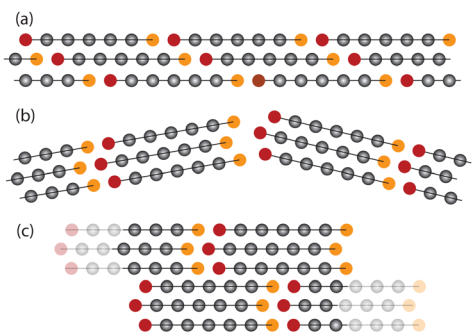


Fig. 14 Minimal model. (a) Filamentous strand composed of three bead-spring chains within its cross-section. Chain ends are marked in red and orange. (b) The strand tends to preferably break when chain ends are aligned, giving rise to two dangling bundles. (c) These bundles join existing strands and thus help to increase their cross-sections (Movie A, ESI†).

Coarsening of network structures has been observed in similar systems and described as either power-law[12] or logarithmic growth.[50] Power law and logarithmic behavior have been associated with two different universality classes of growth kinetics of activated processes, depending on whether the activation barriers grow (logarithmic) or do not grow (power law) with the domain size.[70] While the above arguments seem to favor logarithmic growth, we actually find that both families of fit functions provide equally good descriptions of our data. This indicates that our data do not allow to distinguish between the two universality classes of domain growth advocated in ref. 70. Furthermore, our systems do not exhibit the exponent 0.5 found in the power-law growth of characteristic pore sizes reported for the gas–liquid demixing of colloidal suspensions and simple fluids.[12] Instead, we observe a much weaker exponent of around 0.1 when fitting to power-law behavior. This finding might be taken as a further hint of non-universality of the ultra-slow coarsening kinetics and is in line with recent reports on non-universal aspects regarding the role of elasticity in polymer and colloidal gels.[58] Further investigations on universality classes in ultra-slow coarsening and limits thereof are left for future research.

### 3.5 Anomalous diffusion and relaxational dynamics

The enduring ultra-slow coarsening of these networks poses some challenges for the investigation of their dynamical properties. First and foremost, the lack of time-translational invariance since a stationary state has not been reached implies that we need to carefully distinguish dynamical properties at different waiting times $t_{\mathrm{w}}$ since preparation of the system.

As a first dynamic quantity we study the mean-square displacement (MSD) of bead positions $\Delta(t, t_{\mathrm{w}}) = N_{\mathrm{b}}^{-1} \sum_{j=1}^{N_{\mathrm{b}}} \left[\mathbf{r}_j(t + t_{\mathrm{w}}) - \mathbf{r}_j(t_{\mathrm{w}})\right]^2$ as a function of time $t$ since starting at a given waiting time $t_{\mathrm{w}}$. Fig. 15(a) shows the exemplary case of $\Delta(t,0)$ for $\kappa = 50$ and all 10 independent realizations of the system. For the corresponding $\Delta(t,10^5)$ up to $t = 10^6$ see Fig. S1 (ESI†). Even though each system contains $N_{\mathrm{b}} = 30\,000$ beads, due to the absence of time-averaging, considerable sample-to-sample fluctuations are seen in Fig. 15(a), Fig. S1 (ESI†) and for other values of $\kappa$ (not shown). Closer inspection of trajectories reveals that, except for the relatively early stage ($t_{\mathrm{w}} \lesssim 10^4$), filament fluctuations are rather small with correspondingly small bead displacements. At certain times, however, large reorganizations of the filament networks occur *via* filament breakage and subsequent re-attachment to another strand, leading to very large displacements in some parts of the network over a short time period. Fig. 16 illustrates such a filament breaking event and the corresponding evolution of the MSD for an individual sample in the late stage of coarsening. Similar dynamic heterogeneities occur in a number of different systems, *e.g.* in glass-forming liquids[57] and aging colloidal gels.[17]

We will henceforth focus mostly on the ensemble-averaged MSD $\langle\Delta(t, t_{\mathrm{w}})\rangle$. Fig. 15(b) shows $\langle\Delta(t, t_{\mathrm{w}})\rangle$ for $\kappa = 50$ and three different values of $t_{\mathrm{w}}$. We note that the short-time ballistic

 This journal is © The Royal Society of Chemistry 2025

Open Access Article. Published on 26 February 2025. Downloaded on 6/10/2025 3:11:34 PM.
This article is licensed under a Creative Commons Attribution-NonCommercial 3.0 Unported Licence.

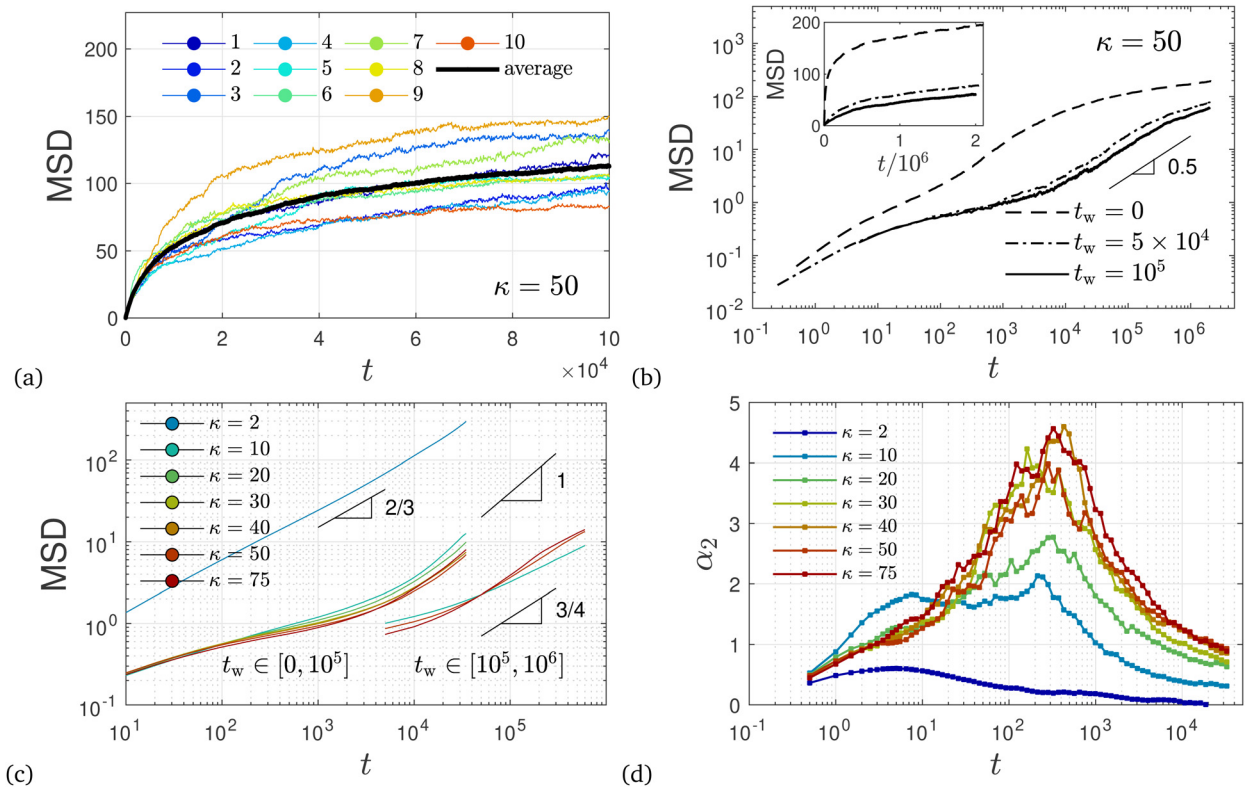


Fig. 15 Mean square bead displacement. (a) MSD $\Delta(t,0)$ up to $t = 10^5$ for $\kappa = 50$ and individual realizations (each sample has its own color). The ensemble average is shown by the black solid line. (b) Ensemble-averaged MSD $\langle\Delta(t, t_w)\rangle$ at three different values for $t_w$ on a double-logarithmic scale (same data on a linear scale are shown in the inset). (c) MSD averaged over two different waiting time intervals: (i) $t_w \in [0,10^5]$ for all $\kappa$ and (ii) $t_w \in [10^5,10^6]$ for $\kappa \in \{10,50,75\}$. All systems, including the unpercolated, flexible system ($\kappa = 2$ shown) seem to approach a diffusive regime only in (A). (d) The non-Gaussian parameter $\alpha_2$ (15) is shown on a semi-logarithmic scale for case (i). For case (ii), the peak of the non-Gaussian parameter $\alpha_2$ grows and occurs at later times.

regime is not visible on the scale shown in Fig. 15(b). Instead, on a double-logarithmic scale, different diffusive regimes can be distinguished in Fig. 15(b), all of them sub-diffusive on the time scale investigated. Moreover, the dynamics is found to be very slow with beads moving only a fraction of their diameter up to times $t \approx 10^3$ except for the case $t_w = 0$. In the regime $t = 5 \times 10^4$ up to $5 \times 10^5$, data seem to follow $\langle\Delta(t, t_w)\rangle \sim t^{0.5}$. In addition, a very significant dynamic slowing down is seen from Fig. 15(b) as the MSD decreases with increasing $t_w$. Similar observations of waiting-time dependence and dynamic slowing down have been made for aging in colloidal gels.[17] At least on a qualitative level, the observed slowing down can in our case be linked to the coarsening network structure investigated above. Before investigating this relation further, we want to point out that ignoring the non-stationary nature of the networks and naively averaging over $t_w$ can lead to wrong conclusions on the diffusive behavior of the system. As an example, Fig. 15(c) shows $\langle\Delta(t, t_w)\rangle$ for various values of bending stiffness $\kappa$, averaged over rather large time intervals at an early $t_w \in [0, 10^5]$ and later stage $t_w \in [10^5, 10^6]$. In this case, the apparent MSD depends strongly on the chosen averaging interval. Moreover, with such averaging, significantly larger values of diffusion exponents are obtained that in some cases may even suggest normal diffusion. Similar artifacts due to inappropriate temporal averages in nonergodic systems are known and have been analyzed within continuous time random walk models with power-law distributed waiting times.[71]

We note that the dynamics observed here bears some similarities to the subdiffusive regime with $\mathrm{MSD}(t) \sim t^{3/4}$ found

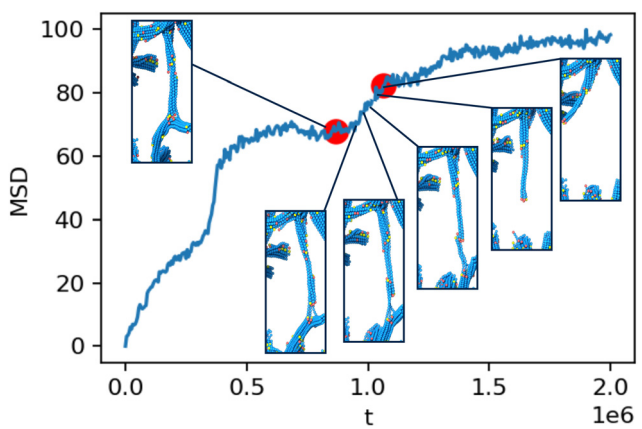


Fig. 16 Filament rupture event. Zoom into a single filament rupture event responsible for the 2nd significant jump in the MSD ($t = 0$ corresponds to $t_w = 10^5$) of an individual sample ($\kappa = 50$, realization 1), recorded at about $t = 1 \times 10^6$ (Movies A–D, ESI†). End beads are colored in red and yellow, as in Fig. 14, all remaining beads are colored in blue.

Open Access Article. Published on 26 February 2025. Downloaded on 6/10/2025 3:11:34 PM.
This article is licensed under a Creative Commons Attribution-NonCommercial 3.0 Unported Licence.

in dilute and entangled solutions of semiflexible polymers.[72,73] For those systems, subdiffusive behavior occurs due to preferential fluctuations perpendicular to the chain contour for inner monomers at short times, before the MSD crosses over to normal diffusion at longer times when the MSD becomes comparable to the polymer size, $\mathrm{MSD}(t) \approx \langle R^2 \rangle$. For our systems, however, almost all chains are part of the temporary network, which leads to a severe hindrance of their mobility. As a consequence, the maximal values of MSD($t$) achieved over the duration of the simulations reported in Fig. 15(c) remain an order of magnitude lower than $\langle R^2 \rangle$. Also for the unpercolated system with $\kappa = 2$, we observe a subdiffusive behavior $\mathrm{MSD}(t) \sim t^{2/3}$, probably due to chain confinement within droplets as discussed in Section 3.2. Some of our observations may support the wormlike bundle model which predicts different dynamic regimes with the MSD perpendicular to the chain contour scaling first as $t^{3/4}$ then $t^{1/2}$ and again $t^{3/4}$, before ultimately approaching a plateau, as this model disregards filament rupture.[74]

To further characterize bead mobility, we refer to the non-Gaussian parameter $\alpha_2$ defined in eqn (15). This quantity (Fig. 15d) characterizes deviations of bead displacements from a Gaussian distribution. For unpercolated systems ($\kappa = 2$), $\alpha_2$ remains small and approaches zero relatively quickly. For percolated systems on the other hand, $\alpha_2$ reaches peak values between 4 and 5 for $\kappa \geq 30$ over an extended period of time around $t \approx 10^2 \ldots 10^3$ before the system enters a different diffusive regime. For larger $t_w$, the peak height of the non-Gaussian parameter grows and moves to later times. Similar peaks in the non-Gaussian parameter have been observed in other systems such as supercooled liquids and glass-forming flexible polymers. In those systems, the peaks in $\alpha_2$ occur near the end of the plateau region of the MSD and have been associated with dynamic heterogeneities due to collective relaxation phenomena such as "cage breaking".[75] Here, however, the peak values observed in $\alpha_2$ are much larger, indicating much stronger deviations from a Gaussian distribution. In addition, although Fig. 15(b) indicates very slow, sub-diffusive dynamics, the MSD is still increasing and does not really plateau at intermediate times. These results are more similar to those found in network liquids[76] and suggest that there are different relaxation mechanisms at work in these percolated networks compared to glassy dynamics, in agreement with recent conclusions.[58] For intermediate values of the bending stiffness at the onset of a percolated network ($\kappa = 10$), an additional peak in $\alpha_2$ is seen from Fig. 15(d). In polymer melts composed of rather rigid chains, the onset of a second peak was seen in computer simulation studies of a model system similar to the one considered here.[77] These authors assumed slow relaxation of nematic domains as the underlying mechanisms of the second peak at late times. Such explanations probably do not carry over to the present case where we observe an additional peak in $\alpha_2$ at earlier times. A double peak in $\alpha_2$ was also seen in computer simulations for a particular choice of parameters in a model for microemulsions, and related to the difference between local cage-breaking *versus* bond relaxation events.[78]

The self part of the intermediate scattering function, $F_s(q, t)$, defined in eqn (14) provides more information on the length-scale dependent relaxational dynamics. See Section 5.3 for more details on this quantity, and Section S1 (ESI†) for a visualization of contributions to $F_s(q, t)$. Fig. 17 shows $F_s(q, t)$ for several (color coded) values of the wave number $q$ over a similar range to those investigated for the static structure factor $S_{sc}(q)$ in Fig. 5. For better visibility, only a tiny fraction of the simulation data are shown as circles in this plot (full datasets available in Fig. S13, ESI†). On small length scales below the bead diameter, *i.e.* $q \gtrsim 6$, relaxation occurs relatively fast and is not much affected by the bending stiffness $\kappa$. On the length scales of the end-to-end distances $R$ of the polymers, corresponding to $q_{ee} = 2\pi/R$, the relaxation of $F_s(q_{ee}, t)$ is generally faster than the orientational end-to-end vector relaxation (see Fig. S8, ESI†), indicating the importance of cooperative effects on these length scales (including the formation locally aligned chains in droplets and bundles). For all systems investigated, relaxation is slowing down by orders of magnitude with decreasing $q$ corresponding to larger length scales. Except for $\kappa = 0$, each panel in Fig. 17 shows two sets of data corresponding to waiting times $t_w = 0$ and $t_w = 10^5$. Relaxation slows down with increasing waiting time, consistent with our observation of dynamic slowing down of the MSD. Such behavior is typical for aging, especially in glassy systems.[79,80] The slowing with increasing $t_w$ is particularly strong for small $q$ values

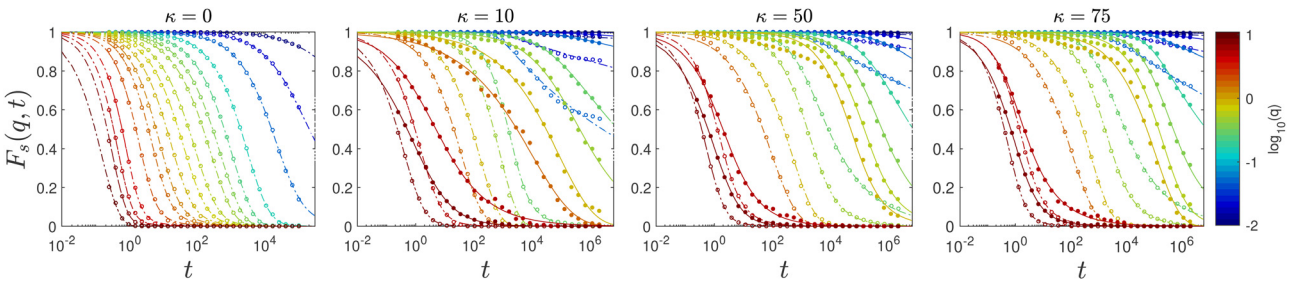


Fig. 17 Incoherent scattering. The time decay of the self part of the intermediate scattering function, $F_s(q, t)$, eqn (14) is shown on a semi-logarithmic scale for selected $q$-values as indicated in the colorbar. Different panels correspond to different values of the bending stiffness $\kappa$ (mentioned in the panel title). In each panel, open and closed circles correspond to $F_s(q, t)$ data for $t_w = 0$ and $t_w = 10^5$, respectively. All lines are fits to the power-ML function (6). The chosen set of $q$ values is not identical for the two $t_w$'s, but they are uniquely color-coded (full data sets available in Fig. S13, ESI†).

 This journal is © The Royal Society of Chemistry 2025

Open Access Article. Published on 26 February 2025. Downloaded on 6/10/2025 3:11:34 PM.
This article is licensed under a Creative Commons Attribution-NonCommercial 3.0 Unported Licence.

($q < 1$), where the intermediate scattering function does not relax to zero on the time scale of the simulations (and would not do so for $q \ll 1$ even if we were to increase the simulation time window by many orders or magnitude). Therefore, we deal with an effective aging and non-ergodic system. This non-ergodic behavior is not only common in colloidal systems with infinite lifetime of bonds,[78] but also reported for real transient networks of semiflexible polymers.[1]

To discuss the relaxation dynamics more quantitatively, we fit the $F_s(q, t)$ simulation data using the "power-ML" function

$$\tilde{F}_s(q,t) = \left[E_\beta\left(-\left(t/\tau'_q\right)^\beta\right)\right]^{\alpha/\beta}, \quad \tau'_q = \left(\frac{\alpha}{\beta^2\Gamma(\beta)}\right)^{1/\beta}\tau_q, \quad (6)$$

where $E_\beta(z) = \sum_{n=0}^{\infty} z^n/\Gamma(1+\beta n)$ denotes the Mittag-Leffler function and $\Gamma(x)$ the Gamma function. For the special case $\alpha = \beta$, eqn (6) reduces to the standard Mittag–Leffler function $E_\beta\left(-\left(t/\tau'_q\right)^\beta\right)$ which is discussed in the literature as the solution to a linear fractional differential equation.[81] By construction, we impose non-negative $E_\beta$, *i.e.* we restrict the fits to $\beta \in [0,1]$. With two exponents $\alpha$, $\beta$ and an effective relaxation time $\tau_q$, our simulation data for $t_w = 0$ and all values of $\kappa$ and $q$ investigated and over seven orders of magnitude in $t$ can be fitted very well by the power-ML function (6), as shown by the close agreement between the lines and open symbols in Fig. 17. For the $t_w = 10^5$ data (filled symbols) eqn (6) does not capture all details in the intermediate time and $q$ ($q \approx 1$) regime.

For relatively early times, $t \ll \tau'_q$, the power-ML function $\tilde{F}_s$ describes a stretched exponential decay $\exp[-(t/\tau_q)^\beta]$, frequently employed to fit relaxation in gels and glasses.[17,78] The corresponding values of the stretching exponents $\beta$ are shown for $t_w = 0$ in Fig. 18(b). A stretching exponent $\beta = 3/4$ was theoretically predicted for solutions of semiflexible polymers.[82] Here we observe a rather large range of $\beta \in [0.6,1]$ values that moreover vary non-monotonically with the wave number $q$. Note that similar values of $\beta$ but in a smaller range [0.6, 0.75] are found if a stretched exponential function is used to fit $F_s(q, t)$ for all times. Those results are not shown since the quality of the corresponding fits is generally inferior to those by the power-ML function. For our model system we can rule out compressed exponential relaxation[17] not only because the power-ML (6) does not allow to capture the $\beta > 1$ regime, but also since $t(\mathrm{d}/\mathrm{d}t)[\ln(-\ln F_s(q, t))]$ does not exceed unity for our measured data, for both $t_w = 0$ and $t_w = 10^5$. From a second-order cumulant expansion, $F_s(q,t) \approx \exp\left[-\left(q^2/6\right)\langle\Delta(t,t_w)\rangle\right]\left(1+\mathcal{O}\left(q^4\right)\right)$, the short-time, small wave vector limit is related to the mean-square diffusion studied above. Our numerical data satisfy this relation (not shown). For times $t \gg \tau'_q$, the power-ML function (6) smoothly interpolates to a power-law behavior, $\tilde{F}_s \sim t^{-\alpha}$, with $\alpha \neq \beta$ in general. Such pronounced power-law behavior is seen in Fig. 17, in particular for small $q$ values. The power-law exponent $\alpha$ obtained from fits to eqn (6) is shown in Fig. 18(a). While for $q \gtrsim 5$, $F_s(q, t)$ decays relatively rapidly so that the behavior is dominated by a stretched-exponential relaxation, relaxation slows down significantly for $q \lesssim 1$ and the power-law regime becomes more and more dominant. Most strikingly, we find that

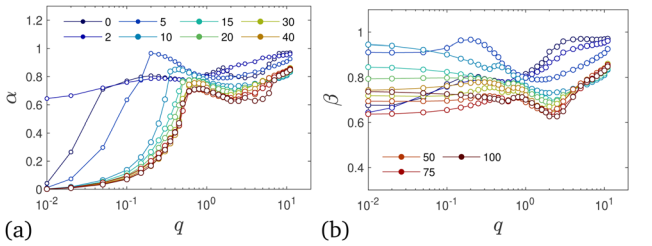


Fig. 18 Power-Mittag–Leffler parameters. (a) Exponent $\alpha$ characterizing the power-law regime at $t \gg \tau'_q$ and (b) exponent $\beta$ characterizing the stretched exponential regime at $t \ll \tau'_q$ of the power-ML function (6) *versus* the wave number $q$ extracted from $F_s(q, t)$ (data symbols in Fig. 17), with additional values of $q$ and $\kappa$ as indicated in the legend. The range of $\kappa$ values shown (legend distributed over both panels) covers the droplet and network phase. Shown are the exponents for $t_w = 0$. For additional details see Fig. S11 and S12 (ESI†).

in this regime the $\alpha$ decreases towards zero with decreasing $q$. While the values of $\alpha$ vary significantly with $\kappa$ for $t_w = 0$, only small variations are seen for $t_w = 10^5$, where approximately $\alpha \sim q^{6/5}$ for $q < 1$ (Fig. S11b, ESI†). Therefore, the long-time relaxation becomes slower and slower on larger scales as the exponent decreases towards zero.

Having clarified short and long-time relaxation regimes, we now turn to a discussion of the characteristic relaxation times. Fig. 19(a) shows the relaxation time $\tau_q$ of the power-ML function (6) governing the time scale of the stretched exponential relaxation. In addition, Fig. 19(b) shows an alternative definition of a relaxation time $\tilde{\tau}_q$ which characterizes the decay of $F_s(q, t)$ to a prescribed level. For convenience we here choose $F_s(q, \tilde{\tau}_q) = 1/2$. For those cases where the simulation data of $F_s(q, t)$ do not decay below 1/2, we use extrapolations from eqn (6) to determine $\tilde{\tau}_q$. While the numerical values of $\tau_q$ and $\tilde{\tau}_q$ are different, both characteristic relaxation times show qualitative similar behavior at large $q$. First, for $t_w = 0$ (open symbols in Fig. 19), the relaxation times show approximately a scaling $q^{-2}$ for $q \gtrsim 10^{-1}$ and the relaxation times are increasing with increasing bending stiffness $\kappa$. Aged systems with $t_w = 10^5$, however, show a rather abrupt increase of $\tau_q$, $\tilde{\tau}_q$ by about three orders of magnitude when $q$

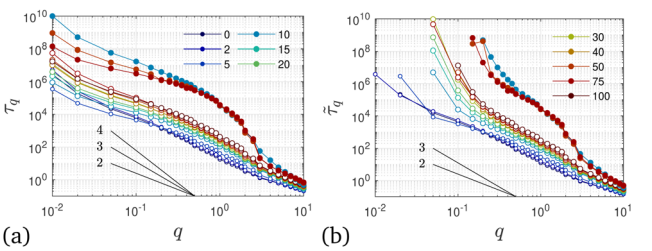


Fig. 19 Effective relaxation times. (a) Characteristic relaxation times $\tau_q$, eqn (6), in the droplet and network phase *versus* the wave number $q$ extracted from the incoherent scattering function (symbols in Fig. 17), with additional values of $q$ and $\kappa$ as indicated in the legend (distributed over both panels). (b) Same as (a) but for the alternative definition of relaxation time $\tilde{\tau}_q$ defined as $F_s(q, \tilde{\tau}_q) = 1/2$. To highlight the dependency of relaxation times on the waiting time, we here display results using $t_w = 0$ (open circles) and $t_w = 10^5$ (filled circles). Not directly measurable $\tilde{\tau}_q$ values had been extrapolated using the $\tilde{F}_s(q, t)$ fits (lines in Fig. 17).

Open Access Article. Published on 26 February 2025. Downloaded on 6/10/2025 3:11:34 PM.
This article is licensed under a Creative Commons Attribution-NonCommercial 3.0 Unported Licence.

decreases from $q \approx 3$ to $q \approx 2$. Interestingly, $\tau_q$, $\tilde{\tau}_q$ are rather insensitive to the precise value of $\kappa$ in the network-forming regime over a relatively large interval of $q$ values. Fig. 19 demonstrates a very rich relaxation behavior of the system that moreover changes significantly between initial ($t_w = 0$) and aged ($t_w = 10^5$) samples. Not only do large structures relax more slowly in these systems, they do so in a particular manner with a $\kappa$-independent onset at a characteristic wave number $q_c$. With $q_c \approx 2...3$, this length scale roughly corresponds to the filament radius $d_f/2$. With relaxation times exceeding $10^6...10^8$ for $q < 10^{-1}$ by far, these systems show ultra-slow relaxation alongside the coarsening behavior established above.

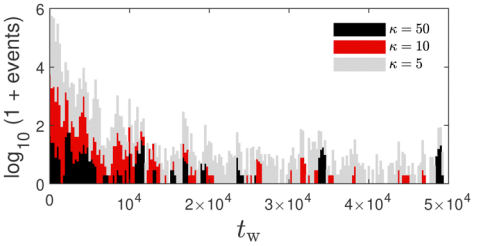


Fig. 20 Reorganization during coarsening. Amount of significant bead displacement events in the course of $t_w$ for $\kappa$ = 5, 10, and 50 for three representative samples. An event we here define to occur, if a bead is displaced by more than 15 within time interval [$t_w$, $t_w$ + 750]. The graph is qualitatively unaffected by this particular choice. Individual spikes appearing for the percolated networks mark the breakage and reorganization of filaments that become more rare as the system coarsens.

# 4 Conclusions

We study systems of semiflexible polymers where cohesive interactions lead to physical, reversible crosslinks. From comprehensive molecular simulations of a generic coarse-grained model, we find polymers to self-assemble into droplets for weak bending stiffness, *i.e.* for relatively flexible chains. For more rigid chains, on the other hand, the interplay between attractive interactions with periodic boundary conditions results in the formation of percolated networks of filaments – a typical behavior observed in many biopolymers.

The self-assembled structures possess well-defined interfaces as evidenced from a pronounced $q^{-4}$ Porod regime of the static structure factor at intermediate scattering values $q$. From a skeleton analysis, we find that the network is dominated by three-fold junctions, with four- or higher-order junctions and dangling ends accounting for a tiny fraction only. We identify the links between junctions as filaments and observe that their mean thickness decreases monotonically with increasing persistence length, in agreement with previous simulation studies,[45] but in contrast with results from scattering experiments on PEG-grafted methylcellulose chains.[22] The resolution of this conundrum is left for future research. We determine the pore size and chord length distribution used to define typical mesh sizes. We find characteristic scaling laws for these systems so that *e.g.* the mean pore radius and the mean filament thickness are proportional to one another.

The systems investigated here show different dynamic regimes of slow, sub-diffusive dynamics with strongly non-Gaussian displacements over a broad time window. In addition, dynamic slowing down is observed as the system ages. The underlying reason for the anomalous diffusion are dynamical heterogeneities due to rare reorganizations of the filament networks with large cooperative displacements of a significant number of beads. The relaxation dynamics is therefore intermittent and dominated by individual events of filament breaking and recombining that become more rare as the system coarsens (Fig. 20). These dynamical heterogeneities are also reflected by stretched exponential and power-law relaxation of the incoherent scattering function, with substantial dynamical slowing down as the system relaxes further. It is important to remark that the incoherent scattering function in the small wave number regime does not decay to zero on the time scale of our simulations. The corresponding lack of ergodicity since large-scale structure are not fully equilibrated has been pointed out also in experiments on gels of amyloid fibers.[1]

We observe a logarithmic dependence on waiting time since system preparation for structural and thermodynamic quantities. This weak logarithmic dependence is easily overlooked when monitoring these quantities on linear scales as is usually done to check for stationarity. Also some quantities like the static structure factor and gyration radius are less sensitive to the ultra-slow relaxation (see Fig. 4 and Fig. S7, ESI†). For other, in particular dynamic, quantities, however, the waiting-time dependence is more significant and naive averaging can lead to incorrect conclusions, *e.g.* regarding the diffusive behavior.

The ultra-slow logarithmic relaxation prevents us from reaching a (approximate) stationary state even with a massive increase in computational resources. The enduring relaxation can be interpreted as an aging process as encountered in many complex and amorphous materials, where the system explores lower and lower potential (bond and bending) energy minima. Structurally, for our system this aging phenomenon involves an ultra-slow coarsening process of network structures where filaments very slowly become thicker while pores become larger. Since both length scales are intimately linked, the ultra-slow coarsening is self-similar in the course of time as evidenced by the very good data collapse onto master curves of the chord length and pore size distributions. It would be interesting to compare these findings with experimental results on aging in comparable biopolymer networks. Exploring the interplay of aging and coarsening with viscoelastic properties of these networks is left for future research.

# 5 Materials and methods

## 5.1 Static structure factors

The static structure factor $S(\mathbf{q})$ is defined by

$$S(\mathbf{q}) = \frac{1}{N_b}\sum_{i,j=1}^{N_b}\left\langle e^{i\mathbf{q}\cdot(\mathbf{r}_i-\mathbf{r}_j)}\right\rangle = \frac{1}{N_b}\left\langle|\delta\rho_{\mathbf{q}}|^2\right\rangle, \quad (7)$$


This journal is © The Royal Society of Chemistry 2025

Open Access Article. Published on 26 February 2025. Downloaded on 6/10/2025 3:11:34 PM.
This article is licensed under a Creative Commons Attribution-NonCommercial 3.0 Unported Licence.

where the double sum runs over all $N_b$ beads in the system and $\delta\rho_q = \sum_{j=1}^{N_b} e^{i\mathbf{q}\cdot\mathbf{r}_j}$ are the Fourier modes of the fluctuating density field. The angular brackets denote ensemble averaging. For isotropic systems, $S$ depends only on the modulus $q = |\mathbf{q}|$ of the wave vector, and can be used to calculate the pair correlation function $g(r) = 1 + (2\pi^2 nr)^{-1}\int_0^\infty q\sin(qr)[S(q)-1]\mathrm{d}q$. We efficiently evaluate $S(q)$ *via* numerical Fourier transform on a $2^{12} \times 2^{12}$ grid to prevent evaluating a double sum or the pair correlation function at large distances (we find that smaller grids lead to inaccurate results in the vicinity of the first minimum of $S(q)$ at about $q = \pi$). The smallest wave vector $q_{min} = 2\pi/L_x$ that we can meaningfully study corresponds to the largest length scale of our system which is the linear size $L_x = V^{1/3}$ of the cubic simulation box. The largest $q_{max} = 4096 q_{min}$ is determined by the chosen grid.

We also evaluate the isotropic scattering function of an individual chain, defined by the Fourier-transformed intramolecular radial pair correlation function[83]

$$S_{sc}(q) = \frac{1}{N}\sum_{i,j=1}^{N}\left\langle e^{i\mathbf{q}\cdot(\mathbf{r}_i-\mathbf{r}_j)}\right\rangle = 1 + \frac{2}{N}\sum_{i,j>i}^{N}\left\langle\frac{\sin(qr_{ij})}{qr_{ij}}\right\rangle \qquad (8)$$

where the double sum runs over all beads of a given chain and the ensemble average includes an average over all chains. By its definition, $S_{sc}(0) = 1 + (N^2 - N)/N = N$. Since $N \ll N_b$, the double sum in eqn (8) can be evaluated directly, and there is no need to calculate the radial pair correlation function. Since unfolded bead coordinates are used, the box size does not limit the range of possible $q$ values, and $S_{sc}(q)$ can be evaluated down to $q = 0$ for any box size $L_x$. The quantity $S_{sc}(q)$ for continuous wormlike-chain with and without excluded volume had been studied theoretically.[84,85]

For discrete WLCs in the absence of excluded volume effects, $S_{sc}$ can be calculated (i) recursively *via* the Laplace-transformed moments of the end-to-end distribution function,[86,87] or (ii) numerically upon generating an ensemble of discrete WLCs, or (iii) analytically using one of the existing approximations for the radially symmetric distribution function $f(L, L_p; R)$ for the end-to-end distance $R$ of a discrete WLC with contour length $L$ and persistence length $L_p$. We here employed the two latter approaches: (ii) to generate an ensemble of $N_c$ discrete WLC with given $N$, $b$ and $\kappa/k_BT$ or $L_p = -b/\ln[\mathscr{L}(\kappa/k_BT)]$ we grow each chain bond by bond, choose bond vector $\mathbf{b}_{j+1} = z\mathbf{b}_j + \mathbf{b}\sqrt{1-z^2}(\mathbf{u}\times\mathbf{b}_j)/|\mathbf{u}\times\mathbf{b}_j|$ with $z = -1 + \ln(1 + c\xi)k_BT/\kappa$, $\xi$ a random number equally distributed on the interval [0,1], $\mathbf{u}$ a random unit vector, and $c = e^{2\kappa/k_BT} - 1$. This algorithm follows from the known distribution of bond angles for the discrete WLC. For huge $\kappa/k_BT > 100$, to prevent numerical precision problems, $z = \max(-1, 1 + \ln(\xi)k_BT/\kappa)$ can be employed instead of the above exact expression. The bead positions, given by $\mathbf{r}_i = \mathbf{r}_{i-1} + \mathbf{b}_i$, are then directly used to evaluate eqn (8). For approach (iii), we start from the highly accurate analytic expression for $f(L, L_p; R)$ proposed by Becker *et al.*,[88] subsequently normalized so that $\int f(L, L_p; R)\mathrm{d}^3R = 1$, and then evaluate the intramolecular pair correlation function $g_{sc}(r)$ by summing over all partial contour distances, *i.e.*, $g_{sc}(r) = N^{-1}\sum_{j=1}^{N}(N-j)f(jb, L_p; r)$. With $g_{sc}(r)$ at hand, we evaluate $S_{sc}(q) = 1 + 4\pi q^{-1}\int_0^L r\sin(rq)[g_{sc}(r) - g_{sc}(L)]\mathrm{d}r$ with $L = (N-1)b$. For the large $L_p > Nb$, approach (iii) runs into numerical problems and we rely on (ii). Both approaches (ii) and (iii) allow us to consider variable bond lengths $b$, but we find that our measured $S_{sc}(q)$ is already well captured over the whole $q$ range including the peaks for $q \gg b^{-1}$, by using a fixed value $b = 1$. As a side-result, we have access to $g_{sc}(r)$ without having to measure this quantity directly.

### 5.2 Effective persistence lengths

We implemented two approaches to extract effective persistence lengths $\ell_p$ and $L_p$ from chain configurations. In the "local" approach, we use the mean bending energy per atom $e_a$, usually reported by LAMMPS (eangle). The corresponding $\ell_p$ is then given by $\ell_p = -b/\ln\langle\mathbf{u}_i\cdot\mathbf{u}_{i+1}\rangle$ with $\langle\mathbf{u}_i\cdot\mathbf{u}_{i+1}\rangle = 1 - Ne_a/[(N-2)\kappa]$. In the second "global" approach we use the ratio between mean squared end-to-end distance $\langle R^2\rangle$ and squared radius of gyration $R_g^2$ of the $N$-chains (Fig. S10, ESI†) and estimate an effective persistence length $L_p$ assuming that the individual chains exhibit the statistics of a discrete WLC (Fig. 21). To this end let us recall the exact analytic expressions for a discrete WLC with $N-1$ bonds and contour length $L = (N-1)b$,[54]

$$\frac{\langle R^2\rangle}{bL} = \frac{1+z}{1-z} - \frac{2z(1-z^{N-1})}{(N-1)(1-z)^2}, \qquad (9)$$

$$\frac{6R_g^2}{bL} = \left[\frac{1+z}{1-z} - \frac{6z}{(N-1)(1-z)^2}\right]\frac{N+1}{N} + \frac{12z[N - z(N+1) + z^{N+1}]}{(1-z)^4(N-1)N^2}, \qquad (10)$$

with $z = e^{-b/L_p}$. Note that the ratio $\langle R^2\rangle/R_g^2$ does depend on $L_p$ only. For $N \gg 1$ and $L_p \gg b$, the discrete WLC converges to the better known continuous WLC characterized by ref. 89

$$\frac{\langle R^2\rangle}{2L_pL} = \frac{L}{2L_p}f_{Debye}(L/L_p), \qquad (11)$$

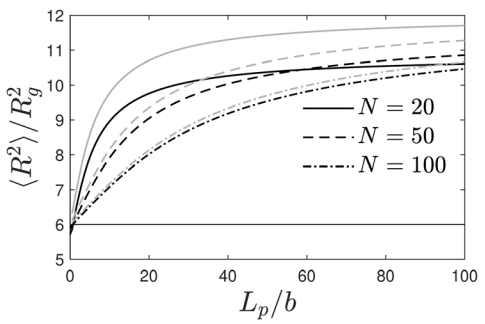


Fig. 21 WLC model prediction. Ratio $\langle R^2\rangle/R_g^2$ *versus* $L_p/b$ for three different $N$ according to eqn (9) and (10) (black) and eqn (11) and (12) (light gray) for comparison. We extract an effective persistence length $L_p$ from this ratio, instead of monitoring the bond–bond correlation function. Alternatively, we extract an effective persistence length $L_p$ by fitting the measured $S_{sc}(q)$ to the discrete WLC model, as described in Section 5.1.

Open Access Article. Published on 26 February 2025. Downloaded on 6/10/2025 3:11:34 PM.
This article is licensed under a Creative Commons Attribution-NonCommercial 3.0 Unported Licence.

$$\frac{6R_g^2}{2L_pL} = 1 - \frac{3L_p}{L}\left[1 - f_{\text{Debye}}\left(L/L_p\right)\right], \tag{12}$$

with the Debye function $f_{\text{Debye}}(x) = 2(e^{-x} + x - 1)/x^2$. In contrast to the continuous WLC, the discrete WLC correctly captures dumbbells, as $\langle R^2\rangle = b^2$ and $R_g^2 = b^2/4$ for $N = 2$. For $\kappa/k_BT \gg 1$ or $L_p/b \gg 1$, $L_p/b \approx \kappa/k_BT$. For an ideal WLC the local $\ell_p$ (obtained from $e_a$) and global $L_p$ (obtained from $\langle R^2\rangle$, $R_g^2$, or their ratio) are identical, and $\ell_p = L_p = L_p^{\text{WLC}}$ with $L_p^{\text{WLC}} = -b/\ln[\mathscr{L}(\kappa/k_BT)]$.

Note that expressions (9) and (10) were written differently, but equivalently, in the mentioned ref. 54. With the nonzero components $A_{13} = -(\pi/2)I_1(L_p/b)/\sinh(L_p/b)$ and $A_{33} = z$ of a $3 \times 3$ matrix $\mathbf{A}$, involving the modified Bessel function $I_1$ of the first kind, the mean squared end-to-end distance was left unevaluated in terms of $\mathbf{A}$ as $\langle R^2\rangle/bL = C_\infty - [2/(N-1)]\cdot[\mathbf{A}\cdot(\mathbf{1} - \mathbf{A}^{N-1})\cdot(1 - \mathbf{A})^{-2}]_{33}$, where $C_\infty = [(\mathbf{1} + \mathbf{A})\cdot(\mathbf{1} - \mathbf{A})^{-1}]_{33}$.

### 5.3 Intermediate scattering function $F(q, t)$

Letting $\mathbf{r}_j(t)$ denote the coordinates of the $j$th bead at time $t$, the intermediate scattering function (also known as dynamic structure factor) is defined by

$$F(\mathbf{q}, t) = \frac{1}{N_b}\langle\delta\rho(\mathbf{q}, t + t_w)\delta\rho(\mathbf{q}, t_w)\rangle, \tag{13}$$

with $\delta\rho(\mathbf{q}, t) = \sum_{j=1}^{N_b}\exp\left[i\mathbf{q}\cdot\mathbf{r}_j(t)\right]$ the instantaneous density fluctuation at wave vector $\mathbf{q}$. For $t = 0$, eqn (13) reduces to the static structure factor $F(\mathbf{q}, 0) = S(\mathbf{q})$ introduced in eqn (7).

We evaluate the radially symmetric self-part of $F(\mathbf{q}, t)$,[90] $F_s(q, t) = \langle\exp[i\mathbf{q}\cdot(\mathbf{r}_j(t + t_w) - \mathbf{r}_j(t_w))]\rangle$, for a selected number of $q$ values. The average is taken over trajectories of 10 statistically independent starting configurations, and all $\mathbf{q}$-vectors with length $q = |\mathbf{q}|$. Such integrals over the unit sphere of orientations of $\mathbf{q}$ vectors amounts to evaluating

$$F_s(q, t) = \left\langle\frac{\sin\left(q\Delta r_j\right)}{q\Delta r_j}\right\rangle, \tag{14}$$

with the bead displacements $\Delta r_j(t) = |\mathbf{r}_j(t + t_w) - \mathbf{r}_j(t_w)|$, and where the average is taken moreover over all $j \in \{1, \ldots, N_b\}$ beads. Eqn (14) refers to the orientation-averaged self-part of the intermediate scattering function.

For small $q$, eqn (14) can be expanded to give[90] $F_s(q, t) = e^{-q^2\langle\Delta r_j^2(t)\rangle/6}\left[1 + q^4\langle\Delta r_j^2(t)\rangle^2\alpha_2(t)/72 + \ldots\right]$, which depends only on the displacements and the non-Gaussian parameter defined by

$$\alpha_2(t) = \frac{3\langle\Delta r_j^4(t)\rangle}{5\langle\Delta r_j^2(t)\rangle^2} - 1. \tag{15}$$

Note that the expansion of $F_s(q, t)$ assumes not only isotropy but also statistical independence of increments, $\langle\Delta r_{j,x}^2(t)\Delta r_{j,y}^2(t)\rangle = \langle\Delta r_{j,x}^2(t)\rangle\langle\Delta r_{j,y}^2(t)\rangle = \langle\Delta r_j^2(t)\rangle^2/9$. We evaluate $\langle\Delta r_j^2(t)\rangle$ and $\langle\Delta r_j^4(t)\rangle$ and calculate $\alpha_2$ directly from eqn (15). For normal diffusion, displacements are Gaussian distributed leading to $\alpha_2 = 0$, while $\alpha_2 \neq 0$ indicates non-Gaussian displacements.

For percolated networks the $F_s(q, t)$, evaluated for $t_w = 0$, exhibits power-law behavior at small $q \lesssim q_c$, and stretched exponential behavior at $q \gtrsim q_c$, where $2\pi/q_c$ is comparable with the filament diameter $d_f$. A class of functions providing the required asymptotic behaviors are the three-parametric Mittag–Leffler functions $f(t) = E_{\alpha,1,\alpha/\beta}\left[-\left(t/\tau_q'\right)^\beta\right]$.[91] Another class, involving the simpler one-parametric Mittag–Leffler function, are the power-ML functions $f(t) = E_\beta\left[-\left(t/\tau_q'\right)^\beta\right]^{\alpha/\beta}$ with $q$-dependent $\beta \in (0,1)$, $\alpha > 0$, $\tau_q' > 0$, which we are using in this work, as they better capture the data. Both versions are characterized by $f(t) = \exp[-(t/\tau_q)^\beta]$ at $t \ll \tau_q'$, and $f(t) = \left(t/\tau_q''\right)^{-\alpha}$ at $t \gg \tau_q'$, while the ratios $\tau_q/\tau_q'$ and $\tau_q''/\tau_q'$ are both uniquely determined by $\alpha$ and $\beta$. For the power-ML one has $\tau_q''/\tau_q' = [1/\Gamma(1-\beta)]^{1/\beta}$ and $\tau_q/\tau_q'$ as stated in eqn (6) already. Due to the existing relationship between $\tau_q$ and $\tau_q''$, it is generally not possible to fit both terminal (early/late) regimes of a measured $F_s(q, t)$ perfectly, and the fitted exponents $\alpha$ and $\beta$ may not coincide exactly with the exponents one would obtain when fitting the asymptotic regimes separately (Section S5, ESI†). This fact must be taken into account when interpreting the exponents.

### 5.4 Network analysis algorithms

**5.4.1 Clusters and critical bonds.** The number of clusters $C$ and their critical bonds (Fig. 22) are extracted from the network composed of permanent and reversible bonds, using available software.[60] The number of critical bonds is the minimum number of bonds that need to be deleted in order to observe depercolation of the system.

**5.4.2 Skeleton.** The length and thickness distribution of filaments, position and functionality of junctions of a given configuration we calculate based on an offlattice-skeleton that we produce using the thinning algorithm described by Gimperlein and Schmiedeberg.[92] Other tools such as Skeleton3D.m[93] require a binary grid and necessitate replicating the original system to mitigate boundary effects; moreover they operate on a resolution that exceeds the bead size and the grid

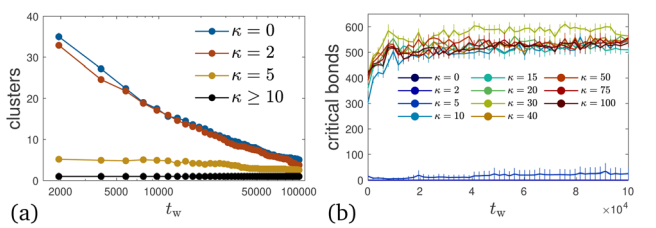


Fig. 22 Clusters and critical bonds. (a) Amount of clusters *versus* waiting time based on graph constructed from the reversible and permanent bonds. (b) Amount of critical bonds. The visible blue line at the figure bottom is for $\kappa = 5$, while there are no critical bonds for $\kappa \leq 2$. The finite number of critical bonds for $\kappa = 5$ stems from the few 1D percolated configurations (Fig. S14, ESI†).

Open Access Article. Published on 26 February 2025. Downloaded on 6/10/2025 3:11:34 PM.
This article is licensed under a Creative Commons Attribution-NonCommercial 3.0 Unported Licence.

makes it difficult to accurately identify junctions. Our skeleton does not suffer from all these disadvantages and is moreover superior in computational efficiency.

The thinning algorithm operates on the bead positions and their permanent and temporary bond information and produces a reduced configuration, the skeleton, upon deleting beads from the original configuration that are identified to not being part of it. The remaining skeleton is free from unattached beads, and made of linear strands connecting junctions. In our implementation, directly connected junctions in the reduced configuration are merged to form a single, higher-functional junction, to prevent the artificial occurrence of filaments with a single bond. The linear strands follow the centerline of the thick filaments and the minimum number of beads that form a loop is the single parameter of the algorithm. While this parameter was chosen as low as 3 in the original work on colloidal gels, and iteratively larger in subsequent works,[94] we use a value of 25. We find that results for the systems under study are basically unaffected by the choice as long as the parameter exceeds 20. Since this skeleton algorithm does not alter the coordinates, and because beads deep inside filaments reside on crystal-like lattices, the linear strands making the skeleton eventually exhibit zig–zag regions. To be able to estimate strand lengths $L_f$ at high precision, as well as their amount $E$, and the total filament length $L_{\text{total}} = EL_f$, we smooth the contour of linear skeleton strands by walking, starting from each junction, along all chains emanating from it up to the next junction (or the chain end), and place each skeleton bead halfway between preceding and next skeleton bead. The adjusted bead positions are then constituting the skeleton, representing the centerlines of the bundles and their junctions (Fig. 12 and Fig. S3, ESI†).

**5.4.3 Edges, loops, and functionalities.** All skeleton beads can be classified according to their functionality $f > 0$. Beads belonging to linear skeleton chains are characterized by $f = 2$, end points by $f = 1$, while $f > 2$ correspond to network junctions (or vertices). Since every $f$-functional junction gives rise to $f$ half filament strands (edges), the total number $E$ of edges connecting $J = \sum_{f=3}^{\infty} n_f$ junctions is given by $E = \sum_f{}' f n_f/2$, where $n_f$ denotes the number of skeleton beads with $f$ neighbors and the summation $\sum'$ runs over all vertices $f$ with $f \neq 2$. For a general network consisting of $C$ disconnected clusters, the total number of independent cycles "loops" $L_\circ$ (also known as circuit rank, cyclomatic number, or nullity of a graph) is determined by the number of edges and vertices as[95,96]

$$L_\circ = E + C - \sum_f{}' n_f, \tag{16}$$

or equivalently, in terms of the number of junctions and dangling strands, $L_\circ = E + C - n_1 - J$. The mean functionality of skeleton beads is $\bar{f} = \sum_{f=1}^{\infty} f n_f / \sum_{f=1}^{\infty} n_f$. The mean junction functionality $\bar{f}_J \equiv \sum_{f=3}^{\infty} f n_f / J$ can alternatively be written as $\bar{f}_J = (2E - n_1)/J$.

**5.4.4 Filament diameters and volumes.** Diameters $d_f$ of the filamentous bundles are not available from the skeleton alone. For each bead residing on a skeleton chain, we calculate $d_f$ by determining the radii in two opposite half-spaces around the bead, where each radius is the minimum distance between the bead center and the void space. The latter is defined as the region that is further away from any bead of the original configuration than $r_\circ = 0.75$. This value is large enough to ensure that there is no void space inside the filaments.

For the calculation of the total polymeric volume $V_f$ and corresponding bead number density $\rho_f = N_b/V_f$, we use a basic Monte Carlo scheme, where we shoot randomly into the simulation box volume $V$. The $V_f$ is then the fraction of shots that hit any of the bead volumes (unchanged radius $r_\circ$), multiplied by $V$. Generally, results for $V_f$ and $d_f$ are sensitive to the choice of $r_\circ$, but at fixed radius we can still evaluate the effect of $\kappa$ and time on the $V_f(t)$ and $d_f(t)$ trajectories.

A rigorous bead number density $\tilde{\rho}_f$ deep inside the filamentous bundles we identify with the mean inverse Voronoi volume of skeleton beads, while the Voronoi construction is performed using all beads. The corresponding polymeric volume, assuming that there is no density gradient inside bundles, is then $\tilde{V}_f = N_b/\tilde{\rho}_f$.

**5.4.5 Pore size distribution.** The physically meaningful[97] geometric pore radius probability density G-$P_{\text{pore}}(r)$ (introduced by Gelb and Gubbins[61]) reported here is a special case of the generalized pore radius distribution GPSD-$P(r; r_p|r_c)$ with probe particle radius $r_p = 0$ and shell thickness $r_c = 0$.[61] We here obtain G-$P_{\text{pore}}(r)$ using the GPSD-3D algorithm with bead (material sphere) radii 0.5.[64] By definition, the cumulative distribution $\text{G-}P_{\text{pore}}^{\text{cum}}(r) = \int_0^r \text{G-}P_{\text{pore}}(r')\mathrm{d}r'$ approaches unity for $r \to \infty$. This G-$P_{\text{pore}}(r)\mathrm{d}r$ is the probability that the largest sphere, containing a randomly chosen point within the void space and not overlapping with the material spheres, has a radius between $r$ and $r + \mathrm{d}r$. The corresponding cumulative pore size distribution is shown in Fig. 9. The mean pore radius is evaluated as $r_{\text{pore}} = \int_0^\infty \text{G-}P_{\text{pore}}(r) r\,\mathrm{d}r$.

A simpler and only marginally related quantity T-$P_{\text{pore}}(r)$ is known as Scheidegger or Torquato-PSD.[63,98] We interpret T-$P_{\text{pore}}(r)$ as the probability of the largest sphere with radius $r$ that can be fitted at a random position within the system without overlapping any material sphere. For comparison, we show in Fig. S9 (ESI†) the cumulative pore size distribution based on T-$P_{\text{pore}}$. By construction, both cumulative pore size distributions are increasing functions. However, clear differences between Fig. 9 and Fig. S9 (ESI†) can be seen, emphasizing the different definitions of both quantities.

**5.4.6 Chord lengths and polymer surface areas.** A chord is defined as the segment between two consecutive intersections of the surface of the fibrous network with a virtual line drawn through the system.[50,66] We determine chord lengths,[65] unweighted ($C_x$) and weighted ($\mathscr{C}_x$) chord length distributions for both the void ($x = 0$) and dense ($x = 1$) phases. Periodic boundaries are taken into account. To define the surface, we consider points in the void space to have a distance exceeding $2r_\circ = 1.5$ from any of the beads. The value 1.5 is large enough to ensure that we do not greatly overestimate the surface area (due to increased roughness at smaller values).

Open Access Article. Published on 26 February 2025. Downloaded on 6/10/2025 3:11:34 PM.
This article is licensed under a Creative Commons Attribution-NonCommercial 3.0 Unported Licence.

Since the probability to choose a point on a chord of length $s$ is proportional to $s$, the weighted and unweighted distributions for the $x$-phase are interrelated by $\mathscr{C}_x(s) \propto s C_x(s)$, with $\int \mathscr{C}_x(s)\mathrm{d}s = 1$. The mean unweighted and weighted chord lengths are then denoted by $l_x = \int s C_x(s)\mathrm{d}s$ and $\ell_x = \int s \mathscr{C}_x(s)\mathrm{d}s$, respectively. The unweighted $C_x(s)$ had been employed in many theoretical works,[57] where one considers all possible chords, while the weighted $\mathscr{C}_x$ is usually extracted by randomly choosing many points inside the $x$-phase, and determining their chord lengths.[12] Analytic expressions exist for some simple geometries like spheres and cylinders.[65] For an ideal cylinder of diameter $d_f$ and length $L_f$ one has $l_1 = d_f L_f/(L_f + d_f/2)$ and $\ell_1 \approx 1.27 \times l_1$.

We extract the chord length distributions with high resolution based on the Cauchy–Crofton formula.[66,99] To this end we generate an ensemble of $X$ lines equally distributed in a large sphere of radius $r_L = \sqrt{3}L_x/2$ and surface area $A_L = 4\pi {r_L}^2$ enclosing the cubic simulation box. Each of the lines connects two random points residing on the surface of the large sphere. This procedure ensures a homogeneous density of an ensemble of $X$ lines within the simulation box volume. For each line, we calculate the number of its intersections with the surface of our filamentous network (including periodic images). Denoting the total number of intersections by $X_f$, the resulting accessible polymer surface area is $A_f = X_f A_L/2X$. The factor 2 accounts for the number of intersections of each line with the surface of the large sphere. As an immediate, but most important by-result one obtains the unweighted distribution of chord lengths, $C_x(s)$, and the weighted distribution $\mathscr{C}_x(s)$ herefrom.

If one were interested in $A_f$ only, it is sufficient to employ a Monte Carlo scheme where one shoots randomly into the surfaces of the $N_\mathrm{b}$ beads defining the void space, and counts the fraction of shots that do not reside inside any of the remaining spheres. This fraction, multiplied by the total surface area of $N_\mathrm{b}$ individual spheres equals $A_f$. We checked that the so-obtained $A_f$ coincides with the $A_f$ from the Cauchy–Crofton approach.

### 5.5 Self-similar coarsening

**5.5.1 Minimal model.** Our minimal model is briefly described in Section 3.4 and schematically depicted in Fig. 14. Consider a one-dimensional, periodic lattice model with $N$ nodes and $N-1$ bonds so that there is exactly one pair of unbonded, adjacent nodes between nodes at positions $x - 1/2$ and $x + 1/2$, say. Such a state characterized by $N$ and $x$ represents parts of two linear chains whose terminal beads meet at $x$. The unbonded pair is considered to perform a random walk on the periodic lattice. A filament with $c$ chains within its cross-section is then represented by a stack of $c$ such one-dimensional lattices, and a set $\{x\}$. Each of the chains, *i.e.*, each of the members of the set is considered to perform an independent random walk. The toy model assumes that a filament breaks as soon as all $x$ values coincide. The members of the destroyed filament then join other filaments, resulting in an increase of the cross-section (diameter $d_f$) of existing filaments. According to this model, the mean rupture time is $\tau_\mathrm{rup}(c) \propto N^{c-1}$, since the probability, that all $c$ unpaired bonds are located, for the first time, at the same position after $s \gg 1$ random steps is $[1-p^{c-1}]^{s-1}p^{c-1}$ with $p = 1/N$. This implies

$$\tau_\mathrm{rup}(c) \propto \frac{\sum_{s=0}^{\infty} s\left[1-p^{c-1}\right]^{s-1}p^{c-1}}{\sum_{s=0}^{\infty}\left[1-p^{c-1}\right]^{s-1}p^{c-1}} = N^{c-1} - 1. \tag{17}$$

In a first approximation, let us assume that the total length of all filaments, $L_\mathrm{total}$, and the mean filament length, $L_f$, are unaffected by $c$. The equation of change for $c$ then reads

$$\frac{\mathrm{d}c}{\mathrm{d}t_\mathrm{w}} = \frac{\Xi c(t_\mathrm{w})}{\tau_\mathrm{rup}(c(t_\mathrm{w}))}, \tag{18}$$

with a factor of proportionality $\Xi$, which is inversely proportional to the number of filaments. The ordinary differential equation (ODE) is solved implicitly, with the help of $\int c^{-1}N^c\,\mathrm{d}c = \mathrm{Ei}(c\ln N)$, by

$$t_\mathrm{w}(c) = \frac{\mathrm{Ei}(c\ln N) - \mathrm{Ei}[c(0)\ln N]}{\Xi N}, \tag{19}$$

where Ei is the exponential integral function.[100] For arguments in the relevant range $x \in [10, 100]$ one has $\mathrm{Ei}(x) \approx \exp(-2.584 + 0.978x)$, and $\mathrm{Ei}^{-1}(y) \approx 2.642 + 1.022\ln(y)$, so that the explicit expression for $c(t_\mathrm{w})$ can be written as

$$c(t_\mathrm{w}) \approx c(0) + \frac{\ln\left[1 + \dfrac{13.25\Xi N t_\mathrm{w}}{N^{0.978c(0)}}\right]}{\ln(N^{0.978})}, \tag{20}$$

which, for not too small times $t_\mathrm{w}$, is of the form $a_\kappa + b_\kappa \ln(t_\mathrm{w})$ that we used to fit the data (Section 5.5.2). Inserting eqn (20) into the expression for $\tau_\mathrm{rup}$ suggests that $\tau_\mathrm{rup}$ increases quasi-linearly with $t_\mathrm{w}$.

This minimal model can be extended to filaments with a length $L_f = mN$ that is a multiple of $N$, *i.e.*, to filaments of diameter $d_\mathrm{f} \propto \sqrt{c}$ that contain $mc$ chains, and $mc$ unpaired bonds. A motivation for this extension is that we know that $L_f$ is roughly proportional to $d_f$, $m \propto \sqrt{c}$. The probability that $c$ unpaired bonds are located, for the first time, at the same position after $s \gg 1$ steps is $[1-p^{c-1}]^{m(s-1)}p^{c-1}[1-p^{c-1}]^{m-1} = [1-p^{c-1}]^{ms-1}p^{c-1}$ with $p = 1/N$, implying $\tau_\mathrm{rup}(c, L_f) = [1-(1-N^{c-1})^{L_f/N}]^{-1} - 1$, keeping in mind that $L_\mathrm{f} \propto \sqrt{c}N$. For $L_f = N\,(m = 1)$ this reduces to the earlier expression. For large $N \gg 1$, $\tau_\mathrm{rup}(c, L_f) \approx m^{-1}N^{c-1}$ is thus by a factor $m \propto \sqrt{c}$ smaller than $\tau_\mathrm{rup}(c)$. Putting this together

$$\frac{\mathrm{d}c}{\mathrm{d}t_\mathrm{w}} = \frac{\Xi\, c^{3/2}(t_\mathrm{w})}{\tau_\mathrm{rup}(c(t_\mathrm{w}))} \tag{21}$$

with another factor of proportionality $\Xi$. This ODE can again be solved for $t_\mathrm{w}(c)$. The inverse $c(t_\mathrm{w})$ grows a little faster than eqn (20), but still logarithmically.

While the minimal model gives rise to logarithmic growth of the number of chains in the cross-section of filaments, it completely ignores length or thickness distributions of filaments, and any variation of the total length of filaments with $c$.

 This journal is © The Royal Society of Chemistry 2025

Open Access Article. Published on 26 February 2025. Downloaded on 6/10/2025 3:11:34 PM.
This article is licensed under a Creative Commons Attribution-NonCommercial 3.0 Unported Licence.

It can thus be improved further to the expense that the corresponding ODE can be solved only numerically.

**5.5.2 Logarithmic fits.** Motivated by the toy model suggesting a logarithmic slow down (20), we use the following fit functions for most of our measured time-dependent quantities due to coarsening,

$$f(t_w) = a_\kappa + b_\kappa \ln(t_w) \quad (t_w \geq 10^4), \tag{22}$$

where $f(t_w)$ is the measured time series, whose two coefficients are well captured using the following dependencies involving four parameters $A_{0,1}$ and $B_{0,1}$,

$$a_\kappa = A_0\left(1 + \frac{10A_1}{\kappa}\right), \quad b_\kappa = B_0\left(1 + \frac{10B_1}{\kappa}\right), \tag{23}$$

so that the corrections proportional to $A_1$ and $B_1$ are, for $\kappa \geq 10$, of particular relevance only if their magnitude is not small compared with unity. Each fit function is fully determined by the four parameters and serves to estimate a quantity for all times $t$, and arbitrary $\kappa$ based on the gathered data. Time averages over a time period $[t_w, t_w + \tau]$ are then given, for arbitrary waiting times $t_w$ by

$$\frac{1}{\tau}\int_{t_w}^{t_w+\tau} f(t)\mathrm{d}t = a_\kappa - b_\kappa\left[1 - \frac{(t_w+\tau)\ln(t_w+\tau) - t_w\ln(t_w)}{\tau}\right]. \tag{24}$$

In this manuscript we necessarily presented results for selected $t_w$ and $\tau$. Since all averages depend on the choice of interval for a system that has not reached equilibrium, eqn (24) can be used to estimate them with the four parameters at hand (Section S8, ESI†). Note that the above form (22) implies $f(t_w) = b_\kappa \ln(t_w/\tau_\kappa)$ with $\tau_k = \exp(-a_\kappa/b_\kappa)$. For large $\kappa \gg 1$, one has

$$\tau_\kappa = \left[1 - 10\frac{A_0}{B_0}(A_1 - B_1)\kappa^{-1} + \mathcal{O}(\kappa^{-2})\right]\mathrm{e}^{-A_0/B_0}. \tag{25}$$

We also tested if our data can be better captured by power-laws, using the modified $f_{\mathrm{pow}}(t_w) = a_\kappa t_w^{b_\kappa}$, where $a_\kappa$ and $b_\kappa$ are again given by eqn (23) but with different values for $A_{0,1}$ and $B_{0,1}$. As a matter of fact, a power-law dependency cannot be ruled out completely. We moreover tested if we can find simple fit functions that capture the various averages much better than the unbounded eqn (22), since most of the measured quantities have an upper or lower bound. We find that the three-parametric rational function $f(t_w) = c_1(1 + c_2x)/(1 + c_3x)$ with $x = \ln(t_w)$ or $x = \ln^2(x)$ serves this purpose, and then allows to estimate a stationary $\lim_{t_w\to\infty} f(t_w) = c_1c_2/c_3$ as well as the time where $f(t_w)$ has reached a certain fraction of its final value. However, such extrapolations to very long times carry a large amount of uncertainty.

**5.5.3 Self-similar $\mathscr{C}_0(s)$ and $\mathscr{C}_1(s)$.** We find that all time-dependent, weighted chord length distributions $\mathscr{C}_x$, multiplied by the characteristic length scale $\ell_x(t)$, fall onto a master curve, if plotted *versus* $s/\ell_x(t)$. This finding is in the same spirit as observations made for other model gels.[12] The multiplication with $\ell_x(t)$ is necessary to keep the normalization intact.

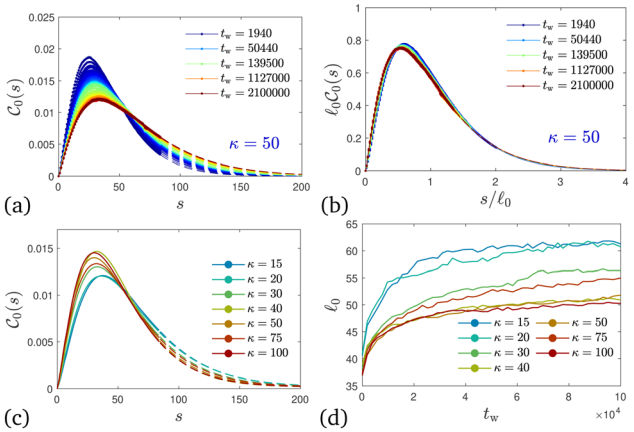


Fig. 23 Distribution and self-similarity of weighted chord lengths. Same as Fig. 10(c)–(f) for the distribution $\mathscr{C}_0(s)$ operating on the void space. The extrapolated lines at $s > L_x$ (dashed) were obtained assuming the form (27) obtained upon studying larger systems with $N_c$ = 50 000 chains.

For our small systems, $\mathscr{C}_0(s)$ as opposed to $\mathscr{C}_1(s)$, does not drop to zero when $s$ reaches the box size $L_x \approx 84.3$. As for $\mathscr{C}_1(s)$ however, the rescaled, measured part of $\mathscr{C}_0(s)$ falls onto a master curve. We use this finding to estimate the full $\mathscr{C}_0(s)$ for all percolated systems by studying a number of large systems with $N_c$ = 50 000 chains (Fig. 19) at unchanged number density for selected $\kappa$ up to relatively small times $t_w = 5 \times 10^4$. For these systems, the box size $L_x \approx 310.7$ is sufficiently large to observe the full $\mathscr{C}_0(s)$ curve. We find that $\mathscr{C}_0(s)$ is (within 2% relative deviation) described by the master curve

$$\mathscr{C}_0(s) = \frac{f_0(s/\ell_0)}{\ell_0}, \quad f_0(x) = \frac{(\nu_0 x\mathrm{e}^{-x})^{\nu_0}}{x\Gamma(\nu_0)}, \tag{26}$$

or equivalently,

$$\mathscr{C}_0(s) = \frac{1}{s\Gamma(\nu_0)}\left(\frac{\nu_0 s}{\ell_0}\mathrm{e}^{-s/\ell_0}\right)^{\nu_0}, \tag{27}$$

which has the proper normalization, $\int\mathscr{C}_0(s)\mathrm{d}s = 1$, and time-dependent first moment $\ell_0 = \int\mathscr{C}_0(s)\mathrm{d}s$ by construction. This $\mathscr{C}_0(s)$ has its maximum at $s_0^{\max} = (\nu_0 - 1)\ell_0/\nu_0$. For the exponent we find $\nu_0 \approx 2.3 \pm 0.1$ for $\kappa = 50$ (large system with $N_c$ = 50 000 chains) and $\nu_0 = 2.4 \pm 0.15$ independent on $\kappa$ for all small systems. For $\nu_0 = 2.3$, $s_0^{\max} \approx 0.63\ell_0$.

For the smaller systems with $N_c$ = 1000 chains, we have measured the un-normalized $\mathscr{C}_0(s)$ up to $s_0^{\max} \leq s \leq L_x$, so that we have already determined $s_0^{\max}$. We then fit the available data to the form (27) to extract $\nu_0$, and herefrom obtain $\ell_0 = \nu_0 s_0^{\max}/(\nu_0 - 1)$.

For $\mathscr{C}_1(s)$ we find the following analytic expression to capture the master curve,

$$\mathscr{C}_1(s) = \frac{f_1(s/\ell_1)}{\ell_1}, \quad f_1(x) = \frac{2\nu_1\cos(\pi/2\nu_1)\left(x/x_1^{\max}\right)^{1+\nu_1}}{x\pi\left[1 + \left(x/x_1^{\max}\right)^{2\nu_1}\right]}, \tag{28}$$

Open Access Article. Published on 26 February 2025. Downloaded on 6/10/2025 3:11:34 PM.
This article is licensed under a Creative Commons Attribution-NonCommercial 3.0 Unported Licence.

or more explicitly,

$$\mathscr{C}_1(s) = \frac{2\nu_1 \cos(\pi/2\nu_1)\left(s/s_1^{\max}\right)^{1+\nu_1}}{s\pi\left[1+\left(s/s_1^{\max}\right)^{2\nu_1}\right]}, \tag{29}$$

where $x_1^{\max}$ and $s_1^{\max}$ are determined by

$$s_1^{\max} = \ell_1 x_1^{\max} = \frac{\ell_1 \cos(\pi/\nu_1)}{\cos(\pi/2\nu_1)}. \tag{30}$$

As before, $s_1^{\max}$ and the prefactors stem from the normalization and $\ell_1 = \int s\mathscr{C}_1(s)\mathrm{d}s$. The maximum of $\mathscr{C}_1(s)$ is achieved at $s = s_1^{\max}$, and the maximum amplitude is $\mathscr{C}_1\left(s_1^{\max}\right) = \nu_1 \cos(\pi/2\nu_1)/\pi s_1^{\max}$ so that we can use the measured $s_1^{\max}$ and $\mathscr{C}_1\left(s_1^{\max}\right)$ to determine both $\nu_1$ and $\ell_1$. For the exponent we find $\nu_1 \approx 2.9 \pm 0.1$ for $\kappa = 50$ (large system with $N_c = 50\,000$ chains) and the same range of value for all $\kappa$ (smaller systems with $N_c = 1000$ chains). For $\nu_1 = 2.9$, $s_1^{\max} \approx 0.6\,\ell_1$.

Just note the identity $C_x(s) = l_x\mathscr{C}_x(s)/s = l_x f_x(s/\ell_x)/s\ell_x$, implying that $C_x(s)$ does not fall onto a master curve except if $\ell_x/l_x$ is a constant at all times. Using the analytic expressions $\mathscr{C}_x$ allows to (i) write $l_x$ as an integral, which we can be evaluated analytically as well (Fig. 24), and (ii) to estimate the scattering intensity, under certain assumptions like convexity,[101,102] which do not strictly apply for our system.

**5.5.4 Scaling relations during coarsening.** In late stages of coarsening where all chains participate in the network, structures where thinner filaments support many smaller pores evolve towards networks with larger pores and thicker filaments. Following arguments put forward by Picu and Sengab[43] we here provide simple scaling arguments to relate filament diameters and pore sizes.

From the skeleton analysis we know the total length of filaments $L_{\text{total}}$ as well as the mean filament diameter $d_f$. Assuming cylindrical filaments where chains are densely packed with cross sectional area fraction $\phi$ (with $\phi = \pi/4$ for the 100-plane of fcc packing), filaments contain on average $c = 4\phi(d_f/\sigma)^2$ different chains within each cross-section, with $\sigma$ an effective bead diameter. Therefore, the total number of chains can be estimated by $N_c \approx cL_{\text{total}}/L_1$ where $L_1 = (N-1)b$ the contour length of a single chain. The simulations confirm that this ratio is indeed constant, independent of $\kappa$. For simplicity of the argument, let us approximate the network structure as a cubic grid with mesh size equal to the mean pore radius $r_{\text{pore}}$. In this case, the total filament length is given by $L_{\text{total}} \approx 3V/r_{\text{pore}}^2$, rather close to $L_{\text{total}} \approx 2V/r_{\text{pore}}^2$ found in the simulations. Inserting into the above relation we find that filament diameter and mean pore size are proportional to each other,

$$d_f = m_1 r_{\text{pore}}, \tag{31}$$

where the prefactor is estimated as $m_1 \approx [\rho b\sigma^2/12\phi]^{1/2}$ with $\rho = N_b/V$ the bead number density introduced above. This agrees with eqn (5). With $\rho = 0.05$, $b = \sigma = 1$, $\phi = 0.5$ we find $m_1 \approx 0.09$. Compared with Fig. 7(g), this value is about a factor of 2 too low. But given the crudeness of the arguments the agreement seems satisfactory. The above arguments do not only apply to late stages of coarsening where both, $d_f$ and $r_{\text{pore}}$, change as function of the waiting time $t_w$. Eqn (31) also applies to well-relaxed network structures for different model parameters such as the bending stiffness $\kappa$.

In a similar spirit, we can estimate the pair energy per particle from interactions within filaments as

$$e_{\text{pair}} \approx \frac{cL_{\text{total}}\bar{z}E_{\text{coh}}}{N_b b} \tag{32}$$

where $\bar{z}$ denotes the average coordination number within a filament. For the bending energy per bond, $e_a$, we assume filaments are approximately straight and bent only at the junctions with an average angle corresponding to $\langle\cos\theta_b\rangle$. Estimating the number of junctions from the number of filaments $E = L_{\text{total}}/L_f$ we find

$$e_a \approx e_{a,1} + \frac{cL_{\text{total}}}{N_b L_f}\kappa(1-\langle\cos\theta_b\rangle), \tag{33}$$

where $e_{a,1} = [N/(N-2)]b\kappa/\ell_p$ accounts for the bending energy of an individual chain in terms of the effective persistence length $\ell_p$ introduced in Section 5.2. Thus, we find that the mean bending energy varies linearly with the pair energy,

$$e_a \approx e_{a,1} + m_2 e_{\text{pair}} \tag{34}$$

with prefactor $m_2$ given by

$$m_2 = \frac{1-\langle\cos\theta_b\rangle}{\bar{z}}\frac{b\kappa}{L_f E_{\text{coh}}}. \tag{35}$$

Assuming the average coordination number $\bar{z}$ and average bending angle between filaments $\langle\cos\theta_b\rangle$ to be approximately constant for late stages of coarsening, eqn (35) suggests that the ratio of pair and bend energy is dictated by the dimensionless parameter $(L_f/b)(E_{\text{coh}}/\kappa)$. Note that a similar parameter was found to govern two-dimensional network structures formed by attractive semiflexible chains.[43] The approximate linear relation (34) between pair and bend energy is in agreement with our observations in Fig. 4(d).

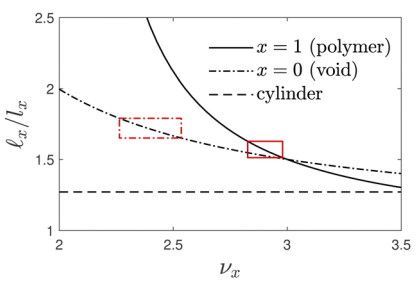


Fig. 24 Mean chord lengths. Ratio between mean weighted and mean unweighted chord lengths *versus* exponent $\nu_x$ with $x \in \{0, 1\}$, predicted by the analytical expressions (27) and (29). The measured ratios range in the regimes marked by the red rectangles. In every case the ratio is larger than the ratio one obtains for cylinders whose height exceeds their radius (dashed). For a sphere $C_1(s) \propto s$ and thus $\ell_1/l_1 = 9/8 = 1.125$.

## Author contributions

C. L.: conceptualization, methodology, software, formal analysis, validation, movies, Fig. 11, 12, 16 and Fig. S2, S3 (ESI†),

 This journal is © The Royal Society of Chemistry 2025

Open Access Article. Published on 26 February 2025. Downloaded on 6/10/2025 3:11:34 PM. This article is licensed under a Creative Commons Attribution-NonCommercial 3.0 Unported Licence.

writing – review & editing; P. I.: conceptualization, formal analysis, validation, writing original draft, writing – review & editing; M. K.: conceptualization, methodology, software, formal analysis, resources, remaining figures, writing – review & editing.

## Data availability

The data supporting this article have been included as part of the ESI.†

## Conflicts of interest

There are no conflicts to declare.

## Acknowledgements

P. I. was supported by EPSRC *via* grant EP/X014738/1 and gratefully acknowledges hospitality of ETH Zürich where part of this research was undertaken.

## Notes and references

1 M. Usuelli, Y. Cao, M. Bagnani, S. Handschin, G. Nystrom and R. Mezzenga, Probing the structure of filamentous nonergodic gels by dynamic light scattering, *Macromolecules*, 2020, **53**, 5950–5956.
2 J. Schnauß, T. Händler and J. Käs, Semiflexible Biopolymers in Bundled Arrangements, *Polymers*, 2016, **8**, 274.
3 K. Tohyama and W. G. Miller, Network structure in gels of rod-like polypeptides, *Nature*, 1981, **289**, 813–814.
4 A. D. Augst, H. J. Kong and D. J. Mooney, Alginate Hydrogels as Biomaterials, *Macromol. Biosci.*, 2006, **6**, 623–633.
5 S. R. Raghavan and J. F. Douglas, The conundrum of gel formation by molecular nanofibers, wormlike micelles, and filamentous proteins: gelation without cross-links?, *Soft Matter*, 2012, **8**, 8539.
6 A. S. G. Van Oosten, M. Vahabi, A. J. Licup, A. Sharma, P. A. Galie, F. C. MacKintosh and P. A. Janmey, Uncoupling shear and uniaxial elastic moduli of semiflexible biopolymer networks: compression-softening and stretch-stiffening, *Sci. Rep.*, 2016, **6**, 19270.
7 M. Arcari, R. Axelrod, J. Adamcik, S. Handschin, A. Sánchez-Ferrer, R. Mezzenga and G. Nyström, Structure–property relationships of cellulose nanofibril hydro- and aerogels and their building blocks, *Nanoscale*, 2020, **12**, 11638–11646.
8 R. C. Picu, Mechanics of random fiber networks–a review, *Soft Matter*, 2011, **7**, 6768.
9 F. Meng and E. Terentjev, Theory of Semiflexible Filaments and Networks, *Polymers*, 2017, **9**, 52.
10 A. G. Zilman and S. A. Safran, Thermodynamics and structure of self-assembled networks, *Phys. Rev. E: Stat., Nonlinear, Soft Matter Phys.*, 2002, **66**, 051107.
11 M. L. Coughlin, L. Liberman, S. P. Ertem, J. Edmund, F. S. Bates and T. P. Lodge, Methyl cellulose solutions and gels: fibril formation and gelation properties, *Prog. Polym. Sci.*, 2021, **112**, 101324.
12 M. Tateno and H. Tanaka, Power-law coarsening in network-forming phase separation governed by mechanical relaxation, *Nat. Commun.*, 2021, **12**, 912.
13 J. Yuan, M. Tateno and H. Tanaka, Mechanical slowing down of network-forming phase separation of polymer solutions, *ACS Nano*, 2023, **17**, 18025–18036.
14 V. Padmanabhan and S. K. Kumar, Gelation in semiflexible polymers, *J. Chem. Phys.*, 2011, **134**, 174902.
15 F. Vargas-Lara and J. Douglas, Fiber Network Formation in Semi-Flexible Polymer Solutions: An Exploratory Computational Study, *Gels*, 2018, **4**, 27.
16 N. Schupper, Y. Rabin and M. Rosenbluh, Multiple Stages in the Aging of a Physical Polymer Gel, *Macromolecules*, 2008, **41**, 3983–3994.
17 P. Chaudhuri and L. Berthier, Ultra-long-range dynamic correlations in a microscopic model for aging gels, *Phys. Rev. E*, 2017, **95**, 060601.
18 M. Manno, D. Giacomazza, J. Newman, V. Martorana and P. L. San Biagio, Amyloid Gels: Precocious Appearance of Elastic Properties during the Formation of an Insulin Fibrillar Network, *Langmuir*, 2010, **26**, 1424–1426.
19 R. Pastore, C. Siviello and D. Larobina, Elastic and Dynamic Heterogeneity in Aging Alginate Gels, *Polymers*, 2021, **13**, 3618.
20 C. P. Broedersz and F. C. MacKintosh, Modeling semiflexible polymer networks, *Rev. Mod. Phys.*, 2014, **86**, 995–1036.
21 J. R. Lott, J. W. McAllister, M. Wasbrough, R. L. Sammler, F. S. Bates and T. P. Lodge, Fibrillar Structure in Aqueous Methylcellulose Solutions and Gels, *Macromolecules*, 2013, **46**, 9760–9771.
22 S. Morozova, P. W. Schmidt, F. S. Bates and T. P. Lodge, Effect of Poly(ethylene glycol) Grafting Density on Methylcellulose Fibril Formation, *Macromolecules*, 2018, **51**, 9413–9421.
23 W. Huang, R. Ramesh, P. K. Jha and R. G. Larson, A Systematic Coarse-Grained Model for Methylcellulose Polymers: Spontaneous Ring Formation at Elevated Temperature, *Macromolecules*, 2016, **49**, 1490–1503.
24 Z. Wu, A. M. Collins and A. Jayaraman, Understanding Self-Assembly and Molecular Packing in Methylcellulose Aqueous Solutions Using Multiscale Modeling and Simulations, *Biomacromolecules*, 2024, **25**, 1682–1695.
25 P. W. Schmidt, S. Morozova, P. M. Owens, R. Adden, Y. Li, F. S. Bates and T. P. Lodge, Molecular Weight Dependence of Methylcellulose Fibrillar Networks, *Macromolecules*, 2018, **51**, 7767–7775.
26 P. W. Schmidt, S. Morozova, S. P. Ertem, M. L. Coughlin, I. Davidovich, Y. Talmon, T. M. Reineke, F. S. Bates and T. P. Lodge, Internal Structure of Methylcellulose Fibrils, *Macromolecules*, 2020, **53**, 398–405.
27 C. L. P. Oliveira, M. A. Behrens, J. S. Pedersen, K. Erlacher, D. Otzen and J. S. Pedersen, A SAXS study of glucagon fibrillation, *J. Mol. Biol.*, 2009, **387**, 147–161.
28 J. S. Pedersen and P. Schurtenberger, Scattering functions of semiflexible polymers with and without excluded volume effects, *Macromolecules*, 1996, **29**, 7602–7612.

Open Access Article. Published on 26 February 2025. Downloaded on 6/10/2025 3:11:34 PM.
This article is licensed under a Creative Commons Attribution-NonCommercial 3.0 Unported Licence.

29 X. Bu and X. Zhang, Scattering and Gaussian Fluctuation Theory for Semiflexible Polymers, *Polymers*, 2016, **8**, 301.
30 L. Jowkarderis and T. G. M. Van De Ven, Mesh size analysis of cellulose nanofibril hydrogels using solute exclusion and PFG-NMR spectroscopy, *Soft Matter*, 2015, **11**, 9201–9210.
31 V. Martorana, S. Raccosta, D. Giacomazza, L. A. Ditta, R. Noto, P. L. San Biagio and M. Manno, Amyloid jams: Mechanical and dynamical properties of an amyloid fibrillar network, *Biophys. Chem.*, 2019, **253**, 106231.
32 A. Rao, H. Yao and B. D. Olsen, Bridging dynamic regimes of segmental relaxation and center-of-mass diffusion in associative protein hydrogels, *Phys. Rev. Res.*, 2020, **2**, 043369.
33 A. Y. Mehandzhiyski and I. Zozoulenko, A Review of Cellulose Coarse-Grained Models and Their Applications, *Polysaccharides*, 2021, **2**, 257–270.
34 B. Strodel, Amyloid aggregation simulations: challenges, advances and perspectives, *Curr. Opin. Struct. Biol.*, 2021, **67**, 145–152.
35 K. Kremer and G. S. Grest, Dynamics of entangled linear polymer melts – A molecular dynamics simulation, *J. Chem. Phys.*, 1990, **92**, 5057–5086.
36 M. Kröger and A. Ben-Shaul, On the presence of loops in linear self-assembling systems, *Cah. Rheol.*, 1997, **16**, 1–6.
37 M. Kröger, Micro/mesoscopic approaches to the ring formation in linear wormlike micellar systems, *Macromol. Symp.*, 1998, **133**, 101–112.
38 R. Faller, A. Kolb and F. Müller-Plathe, Local chain ordering inamorphous polymer melts: influence of chain stiffness, *Phys. Chem. Chem. Phys.*, 1999, **1**, 2071.
39 O. Peleg, M. Kröger, I. Hecht and Y. Rabin, Filamentous networks in phase-separating two-dimensional gels, *Europhys. Lett.*, 2007, **77**, 58007.
40 J. Midya, S. A. Egorov, K. Binder and A. Nikoubashman, Phase behavior of flexible and semiflexible polymers in solvents of varying quality, *J. Chem. Phys.*, 2019, **151**, 034902.
41 J. Zierenberg, M. Marenz and W. Janke, Dilute Semiflexible Polymers with Attraction: Collapse, Folding and Aggregation, *Polymers*, 2016, **8**, 333.
42 T. Arcangeli, T. Skrbic, S. Azote, D. Marcato, A. Rosa, J. R. Banavar, R. Piazza, A. Maritan and A. Giacometti, Phase Behavior and Self-Assembly of Semiflexible Polymers in Poor-Solvent Solutions, *Macromolecules*, 2024, **57**, 8940–8955.
43 R. C. Picu and A. Sengab, Structural evolution and stability of non-crosslinked fiber networks with inter-fiber adhesion, *Soft Matter*, 2018, **14**, 2254–2266.
44 Y. Zhang, E. P. DeBenedictis and S. Keten, Cohesive and adhesive properties of crosslinked semiflexible biopolymer networks, *Soft Matter*, 2019, **15**, 3807–3816.
45 E. P. DeBenedictis, Y. Zhang and S. Keten, Structure and Mechanics of Bundled Semiflexible Polymer Networks, *Macromolecules*, 2020, **53**, 6123–6134.
46 A. Jüngel, *Polymer Chains and Networks: Statistical Foundations and Computer Simulations*, Oxford University Press, UK, 2005.
47 R. D. Groot, Mesoscale simulation of semiflexible chains. II. Evolution dynamics and stability of fiber bundle networks, *J. Chem. Phys.*, 2013, **138**, 224904.
48 P. N. Depta, P. Gurikov, B. Schroeter, A. Forgács, J. Kalmár, G. Paul, L. Marchese, S. Heinrich and M. Dosta, DEM-Based Approach for the Modeling of Gelation and Its Application to Alginate, *J. Chem. Inf. Model.*, 2022, **62**, 49–70.
49 R. Bandyopadhyay, D. Liang, J. L. Harden and R. L. Leheny, Slow dynamics, aging, and glassy rheology in soft and living matter, *Solid State Commun.*, 2006, **139**, 589–598.
50 S. C. Volpe, D. Leporini and F. Puosi, Structure and Mechanical Properties of a Porous Polymer Material via Molecular Dynamics Simulations, *Polymers*, 2023, **15**, 358.
51 S. Plimpton and B. Hendrickson, A new parallel method for molecular dynamics simulation of macromolecular systems, *J. Comput. Chem.*, 1996, **17**, 326–337.
52 H. R. Warner, Kinetic theory and rheology of dilute suspensions of finitely extendible dumbbells, *Ind. Eng. Chem. Fundam.*, 1972, **11**, 379–387.
53 M. Kröger, Simple, admissible, and accurate approximants of the inverse Langevin and Brillouin functions, relevant for strong polymer deformations and flows, *J. Non-Newt. Fluid Mech.*, 2015, **223**, 77–87.
54 O. Weismantel, A. A. Galata, M. Sadeghi, A. Kröger and M. Kröger, Efficient generation of self-avoiding, semiflexible rotational isomeric chain ensembles in bulk, in confined geometries, and on surfaces, *Comput. Phys. Commun.*, 2022, **270**, 108176.
55 Y. Xu, Y. Hamada and T. Taniguchi, Multiscale simulations for polymer melt spinning process using Kremer–Grest CG model and continuous fluid mechanics model, *J. Non-Newt. Fluid Mech.*, 2024, **325**, 105195.
56 O. Lieleg, J. Kayser, G. Brambilla, L. Cipelletti and A. R. Bausch, Slow dynamics and internal stress relaxation in bundled cytoskeletal networks, *Nat. Mater.*, 2011, **10**, 236–242.
57 V. Testard, L. Berthier and W. Kob, Intermittent dynamics and logarithmic domain growth during the spinodal decomposition of a glass-forming liquid, *J. Chem. Phys.*, 2014, **140**, 164502.
58 Y. Wang, M. Tateno and H. Tanaka, Distinct elastic properties and their origins in glasses and gels, *Nat. Phys.*, 2024, **20**, 1171–1179.
59 S. Ciccariello and J. Brumberger, On the Porod law, *J. Appl. Crystallogr.*, 1988, **21**, 117.
60 S. Agrawal, S. Galmarini and M. Kröger, Energy formulation for infinite structures: order parameter for percolation, critical bonds and power-law scaling of contact-based transport, *Phys. Rev. Lett.*, 2024, **132**, 196101.
61 L. D. Gelb and K. Gubbins, Pore Size Distributions in Porous Glasses: A Computer Simulation Study, *Langmuir*, 1999, **15**, 305–308.
62 Y. Masubuchi, Phantom chain simulations for fracture of end-linking networks, *Polymer*, 2024, **297**, 126880.
63 S. Torquato, B. Lu and J. Rubinstein, Nearest-neighbor distribution functions in many-body systems, *Phys. Rev. A: At., Mol., Opt. Phys.*, 1990, **41**, 2059.
64 M. Kröger, S. Agrawal and S. Galmarini, Generalized geometric pore size distribution code GPSD-3D for periodic

 This journal is © The Royal Society of Chemistry 2025

Open Access Article. Published on 26 February 2025. Downloaded on 6/10/2025 3:11:34 PM.
This article is licensed under a Creative Commons Attribution-NonCommercial 3.0 Unported Licence.

systems composed of monodisperse spheres, *Comput. Phys. Commun.*, 2024, **301**, 109212.
65 W. Gille, *Particle and particle systems characterization: small-angle scattering (SAS) applications*, CRC Press, 2013.
66 L. D. Gelb and K. Gubbins, Characterization of porous glasses: simulation models, adsorption isotherms, and the Brunauer–Emmett–Teller analysis method, *Langmuir*, 1998, **14**, 2097–2111.
67 G. Ruben, Intraneuronal Neurofibrillary Tangles Isolated from AlzheimerDisease Affected Brains Visualized by Vertical Platinum-Carbon Replication for TEM, *Microsc. Microanal.*, 1997, **3**, 47–48.
68 M. Usuelli, T. Germerdonk, Y. Cao, M. Peydayesh, M. Bagnani, S. Handschin, G. Nyström and R. Mezzenga, Polysaccharide-reinforced amyloid fibril hydrogels and aerogels, *Nanoscale*, 2021, **13**, 12534–12545.
69 A. Stukowski, Visualization and analysis of atomistic simulation data with OVITO-the Open Visualization Tool, *Modell. Simul. Mater. Sci. Eng.*, 2010, **18**, 015012.
70 Z. W. Lai, G. F. Mazenko and O. T. Valls, Classes for growth kinetics problems at low temperatures, *Phys. Rev. B: Condens. Matter Mater. Phys.*, 1988, **37**, 9481–9494.
71 A. Lubelski, I. M. Sokolov and J. Klafter, Nonergodicity mimics inhomogeneity in single particle tracking, *Phys. Rev. Lett.*, 2008, **100**, 250602.
72 A. Nikoubashman, A. Milchev and K. Binder, Dynamics of single semiflexible polymers in dilute solution, *J. Chem. Phys.*, 2016, **145**, 234903.
73 P. Lang and E. Frey, Disentangling entanglements in biopolymer solutions, *Nat. Commun.*, 2018, **9**, 494.
74 C. Heussinger, F. Schüller and E. Frey, Statics and dynamics of the wormlike bundle model, *Phys. Rev. E: Stat., Nonlinear, Soft Matter Phys.*, 2010, **81**, 021904.
75 W.-S. Xu, J. F. Douglas and K. F. Freed, Influence of Cohesive Energy on Relaxation in a Model Glass-Forming Polymer Melt, *Macromolecules*, 2016, **49**, 8355–8370.
76 S. Roldán-Vargas, L. Rovigatti and F. Sciortino, Connectivity, dynamics, and structure in a tetrahedral network liquid, *Soft Matter*, 2017, **13**, 514–530.
77 H. T. Nguyen and R. S. Hoy, Effect of chain stiffness and temperature on the dynamics and microstructure of crystallizable bead-spring polymer melts, *Phys. Rev. E*, 2016, **94**, 052502.
78 P. Chaudhuri, P. I. Hurtado, L. Berthier and W. Kob, Relaxation dynamics in a transient network fluid with competing gel and glass phases, *J. Chem. Phys.*, 2015, **142**, 174503.
79 W. Kob and J.-L. Barrat, Fluctuations, response and aging dynamics in a simple glass-forming liquid out of equilibrium, *Eur. Phys. J. B*, 2000, **13**, 319–333.
80 W. Kob and J.-L. Barrat, Aging Effects in a Lennard-Jones Glass, *Phys. Rev. Lett.*, 1997, **78**, 4581–4584.
81 F. Mainardi, On some properties of the Mittag-Leffler function $E_\alpha(-t^\alpha)$, *Discr. Contin. Dyn. Syst. B*, 2013, **19**, 2267–2278.
82 K. Kroy and E. Frey, Dynamic scattering from solutions of semiflexible polymers, *Phys. Rev. E: Stat. Phys., Plasmas, Fluids, Relat. Interdiscip. Top.*, 1997, **55**, 3092–3101.
83 J. Higgins, H. Benot and H. Benot, *Polymers and Neutron Scattering*, Clarendon Press, New York, 1996.
84 J. des Cloizeaux, Form Factor of an Infinite Kratky-Porod Chain, *Macromolecules*, 1973, **6**, 403–407.
85 Y. Nakamura and T. Norisuye, Scattering function for wormlike chains with finite thickness, *J. Polym. Sci., Part B:Polym. Phys.*, 2004, **42**, 1398–1407.
86 A. J. Spakowitz and Z.-G. Wang, Exact Results for a Semiflexible Polymer Chain in an Aligning Field, *Macromolecules*, 2004, **37**, 5814–5823.
87 A. J. Spakowitz, *PhD thesis*, California Institute of Technology, 2005.
88 N. Becker, A. Rosa and R. Everaers, The radial distribution function of worm-like chains, *Eur. Phys. J. E:Soft Matter Biol. Phys.*, 2010, **32**, 53–69.
89 O. Kratky and G. Porod, Röntgenuntersuchung gelöster fadenmoleküle, *Recl. Trav. Chim. Pays-Bas*, 1949, **68**, 1106–1122.
90 W. Van Megen, T. C. Mortensen, S. R. Williams and J. Müller, Measurement of the self-intermediate scattering function of suspensions of hard spherical particles near the glass transition, *Phys. Rev. E: Stat. Phys., Plasmas, Fluids, Relat. Interdiscip. Top.*, 1998, **58**, 6073–6085.
91 K. Górska, A. Horzela and K. A. Penson, Non-Debye Relaxations: The Ups and Downs of the Stretched Exponential vs. Mittag-Lefflers Matchings, *Fract. Fractional*, 2021, **5**, 265.
92 M. Gimperlein and M. Schmiedeberg, Structural and dynamical properties of dilute gel networks in colloid–polymer mixtures, *J. Chem. Phys.*, 2021, **154**, 244903.
93 P. Kollmannsberger, M. Kerschnitzki, F. Repp, W. Wagermaier, R. Weinkamer and P. Fratzl, The small world of osteocytes: connectomics of the lacuno-canalicular network in bone, *New J. Phys.*, 2017, **19**, 073019.
94 K. Hirata and T. Araki, Formation dynamics of branching structure in the slippery DLCA model, *J. Chem. Phys.*, 2024, **160**, 234901.
95 R. J. Trudeau, *Dots and Lines*, Kent State University Press, United States, 1976.
96 C. Berge, *Cyclomatic number, The Theory of Graphs*, Courier Dover Publications, 2001, pp. 27–30.
97 M. M. Tomadakis and T. J. Robertson, Pore size distribution, survival probability, and relaxation time in random and ordered arrays of fibers, *J. Chem. Phys.*, 2003, **119**, 1741–1749.
98 A. E. Scheidegger, *The Physics of Flow Through Porous Media*, University of Toronto Press, Toronto, Canada, 1957, p. 7.
99 Y.-S. Liu, J. Yi, H. Zhang, G.-Q. Zheng and J.-C. Paul, Surface area estimation of digitized 3D objects using quasi-Monte Carlo methods, *Pattern Recogn.*, 2010, **43**, 3900–3909.
100 M. Abramowitz and I. A. Stegun, *Handbook of Mathematical Functions*, Dover Publ., New York, 1970.
101 P. Levitz and D. Tchoubar, Disordered porous solids: from chord distributions to small angle scattering, *J. Phys. I*, 1992, **2**, 771–790.
102 C. J. Gommes, Y. Jiao, A. P. Roberts and D. Jeulin, Chord-length distributions cannot generally be obtained from small-angle scattering, *J. Appl. Crystallogr.*, 2020, **53**, 127–132.